Doctoral Thesis

Bioinspired Nanocomposite Adhesives Based on 3D Microarchitectures and 1D Nanomaterials for Advanced Thermal and Electrical Applications

Minho Seong

Department of Mechanical Engineering

(Mechanical Engineering)

Ulsan National Institute of Science and Technology

2021

Bioinspired Nanocomposite Adhesives Based on 3D Microarchitectures and 1D Nanomaterials for Advanced Thermal and Electrical Applications

Minho Seong

Department of Mechanical Engineering

(Mechanical Engineering)

Ulsan National Institute of Science and Technology

Bioinspired Nanocomposite Adhesives Based on 3D Microarchitectures and 1D Nanomaterials for Advanced Thermal and Electrical Applications

A thesis/dissertation submitted to

Ulsan National Institute of Science and Technology

in partial fulfillment of the

requirements for the degree of

Doctor of Philosophy

Minho Seong

12/09/2020

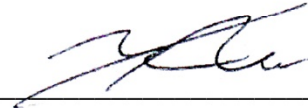Approved by

_____

Advisor

Hoon Eui Jeong

Bioinspired Nanocomposite Adhesives Based on 3D Microarchitectures and 1D Nanomaterials for Advanced Thermal and Electrical Applications

Minho Seong

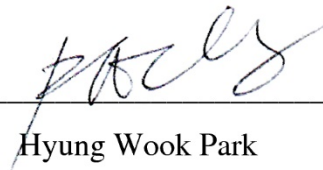This certifies that the thesis/dissertation of Minho Seong is approved.
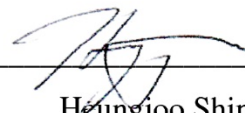
12/09/2020

_____

Advisor: Hoon Eui Jeong

_____

Taesung Kim

_____

Hyung Wook Park

_____

Heungjoo Shin

_____

Moon Kyu Kwak

Abstract

Functional adhesives are essential components in a variety of application fields from daily life to high-tech industries, including precision manufacturing, aerospace, flexible electronics, and wearable devices. However, conventional functional adhesives based on chemically reactive, hot-melt, and viscoelastic adhesive materials generally form uncontrollable mechanical contact, producing bulky, contaminated, or damaged contact interfaces. To address these issues, bioinspired adhesive architectures exhibiting robust, reversible, and residue-free adhesion properties have been proposed. The extraordinary adhesion properties are due to the presence of nano- or micro-hair arrays with protruding tips that maximize van der Waals interactions between surfaces. The photolithography process followed by the replica-molding process has allowed the production of bioinspired artificial adhesives with robust adhesion and high structural stability in a simple, precise, and highly reproducible way. Nevertheless, the manufacturing process narrows the selection of materials to thermal- or UV-curable polymers whose inherently poor thermomechanical and electrical properties hinder the application of bioinspired adhesives in advanced industrial fields.

One-dimensional (1D) nanomaterials including carbon nanotubes (CNTs), metallic nanowires, and nanorods have been actively studied as nanofillers to enhance the mechanical, electrical, and thermal properties of polymeric materials. Yet, the existing methods for the application of nanomaterials are not suitable for fabricating three-dimensional (3D) microarchitectures since the high viscosity of nanomaterial–polymer mixtures inhibits the successful formation of the structures. Furthermore, the rough morphology of the nanomaterials hinders the formation of intimate contact interfaces resulting in low adhesion strength.

In this dissertation, we present novel design strategies for bioinspired nanocomposite adhesives, in which 1D nanomaterials are integrated into 3D microarchitectures. The strategies include microarchitecture designs, nanomaterial selections, and optimization of integration processes that allow microarchitectures to have enhanced thermal or electrical properties while maintaining superior adhesion performance.

In Chapter 2, we propose high-temperature compatible adhesives based on an integration of mushroom-shaped microarchitectures and CNT-based nanocomposites. The nanocomposite microarchitectures are prepared by a photolithography process followed by replica-molding techniques in which polydimethylsiloxane (PDMS) matrices are reinforced with CNT fillers. The excellent thermomechanical properties of the CNTs enable the mushroom-shaped adhesive architectures to have exceptionally enhanced thermomechanical stability compared to pristine PDMS. Moreover, the manufactured adhesives exhibit robust adhesion performances even when exposed to elevated temperatures of ~350 °C; thus, they could be utilized as versatile high-temperature compatible adhesives with high reversibility.

In Chapter 3, we propose a flexible, transparent, and electrically conductive adhesive composed of tentacle-like adhesive architectures and selectively coated percolating silver nanowires (AgNWs). The integrated design provides robust mechanical and low-resistance electrical contacts by forming intimate contact interfaces. The contact interfaces enable efficient electrical connections with active electrodes through attachment without the use of additional contact processes such as mechanical clamping, chemical adhesives, or vacuum deposition, with the contact remaining stable even when highly bent. The superior features of bioinspired conductive adhesives are demonstrated in self-attachable transparent heaters that can form a direct, seamless contact between its AgNWs and the target substrates, providing direct heat-transfer pathways for precise temperature control of the substrate while minimizing energy loss.

Keywords: Adhesion, Bioinspired adhesives, Nanocomposites, Silver nanowires, Carbon nanotubes

Contents

List of Figures

List of Tables

Nomenclature

Abbreviations

Au	Gold
Ag	Silver
Cu	Copper
Ni	Nickel
Si	Silicon
Pt	Platinum
HMA	Hot-melt adhesive
PSA	Pressure-sensitive adhesive
1D	One dimension
3D	Three dimensions
PU	Polyurethane
PUA	Polyurethane acrylate
PDMS	Polydimethylsiloxane
CNT	Carbon nanotube
MWCNT	Multiwalled carbon nanotube
AgNW	Silver nanowire
LOR	Lift-off resist
PR	Photoresist
SEM	Scanning electron microscopy
TGA	Thermogravimetric analysis
DTG	Derivative thermogravimetry
MDRT	Maximum decomposition rate temperature
CA	Contact angle
DI water	Deionized water
FTCE	Flexible and transparent conductive electrodes

ITO	Indium tin oxide
AF-TCE	Self-attachable, flexible, transparent, and conductive electrode
e-PUA	Elastic polyurethane acrylate
EDS	Energy dispersive spectroscopy
AFM	Atomic force microscopy
G	Grid electrode
GT	Grid electrode with tentacles
GTT	Grid electrode with tentacles and tips
FEA	Finite element analysis
PET	Polyethylene terephthalate
LED	Light-emitting diode
BPA(EO)10DMA	Bisphenol A (ethoxylated) 10 dimetacrylate
SMD	Surface mount device
UV	Ultraviolet
NIR	Near-infrared
IR	Infrared
UV-Vis-NIR	Ultraviolet-visible-near-infrared spectroscopy
CZM	Cohesive zone model
RVE	Representative volume element

List of symbols

σ	Adhesion strength
W	Work of adhesion
E	Elastic modulus
R	Radius of pillar
v	Poisson's ratio
P	Pull off force
N	Number of pillars

P_P	Preload
K	Effective Young's modulus
γ	Surface tension
γ^d	Dispersive components of the surface tension
γ^p	Polar components of the surface tension
f	Filling factor
w	Width of the grid pattern
s	Spacing of the grid pattern
T	Transmittance
R_s	Sheet resistance
T_i	Transmittance of the uncoated grid
T_{film}	Transmittance of the coated film
Z_0	Characteristic impedance
σ_{op}	Optical conductivity
t_c	Critical thickness
n	Percolation exponent
$\sigma_{DC,B}$	Bulk DC conductivity

Chapter 1. Introduction

1-1. Research Background

1-1-1. Functional Adhesives

Functional adhesives are adhesives with advanced properties, such as high durability, impact resistance, thermal stability, or electrical conductivity.[1-4] They are essential components of a wide range of applications ranging from daily life to advanced industries, including precision manufacturing, aerospace devices, and flexible electronics.[5-7] High-temperature compatible adhesives are used to maintain close and intimate physical contact between two surfaces at high temperatures (> 150 °C).[4] The most widely used commercial product of this type is a Kapton tape consisting of silicon adhesives with polyimide films.[8,9] The composition provides high thermal stability up to 250 °C as well as superior chemical resistance, which enables it to be utilized in various high-temperature precision manufacturing processes. Electrically conductive adhesives are used to form intimate electrical contacts or junctions between active components of electrical devices. For this purpose, composite adhesives with conductive metallic (Au, Ag, Cu, and Ni) or carbon fillers are mainly utilized.[2,10] These conductive adhesives enable easy and fast electrical connections, grounding, and electromagnetic shielding. The development of various advanced industries is expected to increase the demand for functional adhesives with excellent thermal and electrical properties.

Conventional adhesives are commonly organized into two broad classes: reactive and non-reactive. The chemically reactive adhesives bond two surfaces through chemical reactions that require pre-mixing two polymers or additional external stimuli (UV, heat, moisture).[11,12] Typical non-reactive types are hot-melt adhesives (HMAs) and pressure-sensitive adhesives (PSAs).[13,14] HMAs are composed of thermoplastic materials that require high temperatures for bonding two surfaces. PSAs require uniform pressure for strong adhesion since their performance relies only on their viscoelasticity. Although these conventional methods can form strong mechanical adhesion between the surfaces, they have the following three limitations. First, additional solvents, heat, or pressure required for chemical reaction or hardening can damage the surfaces; thus such adhesives are not suitable for stimuli-sensitive substrates (e.g., skin). Second, the tacky nature of adhesives leaves residues on the surface after removal, which causes contamination or defects, lowering productivity, especially in continuous manufacturing processes.[8] Third, they have low reusability that may cause increased production costs and potential environmental problems. To overcome these limitations, new adhesives that form robust, damage-free, clean, and highly reusable contact interfaces with diverse substrates are in demand.

1-1-2. Bioinspired Adhesives with 3D Microarchitectures

Nature has various contact mechanisms in biological systems.[15-21] Among the various species, gecko lizards, beetles, flies, and spiders have extraordinary adhesive properties of robust, reversible, and directional adhesion on their toes (**Figure 1.1**).[15,22-24] They attach themselves to and move on vertical walls or ceilings while bearing their body weight as well as without leaving any sticky residues. Over the last several decades, many studies have reported that their extraordinary adhesion is due to their unique toe surface topographies, which are millions of arrays of micro- and nanoscopic foot hairs (setae) with protruding tip structures.[24] The unusual adhesion capability, called dry adhesion, works according to the combination of the hairs and tips. The hairy structures with a high aspect ratio maximize the van der Waals interactions since they can be conformally and closely attached to the substrates based on the contact splitting effects.[23] Tip structures extruded from the end of the hairs enhance the adhesion by increasing the contact area and distributing stress uniformly at the contact interface.[25] During removal, independently attached hairs withstand higher stress until they are separated since stored elastic repulsive energy is not easily transferred to the near hairs.[26,27] Based on the described mechanism, the patterned surface with hairy arrays with protruding tips has strong, infinitely usable, and clean adhesion-forming residue- or damage-free contact interfaces with various substrates.
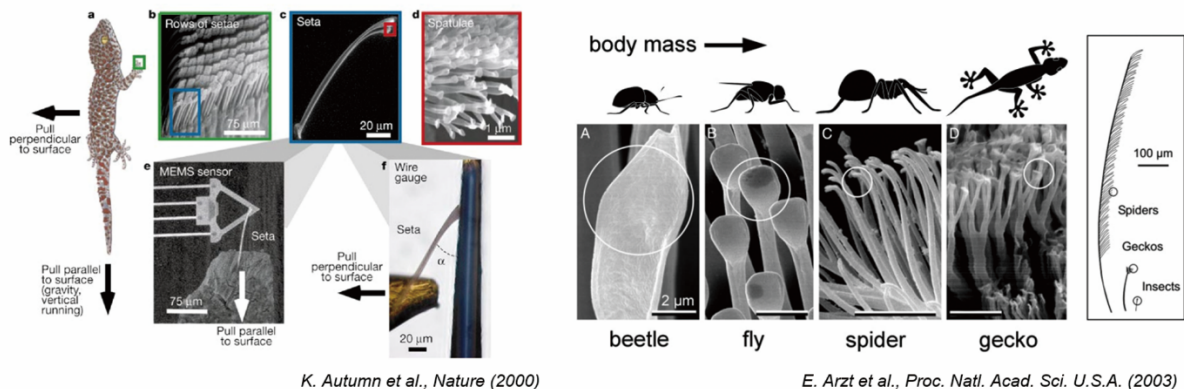
Figure 1.1. Micro- and nanoscale terminal structures for dry adhesion mechanism in various biological systems. Reproduced with permission from ref.[24] © 2000 Springer. Reproduced with permission from ref.[23] © 2003 National Academy of Sciences.

To mimic the contact mechanism of dry adhesives, extensive studies on the artificial adhesive architectures were conducted.[28-30] Early research aimed to realize the excellent adhesion of dry adhesives by synthesizing micro- or nano-hair arrays using polymeric materials. The polymer-based artificial hair or pillar arrays have been fabricated by top-down fabrication techniques, such as photolithography, electron-beam lithography, and soft lithography. The development of the fabrication

process enables precise control over structural parameters of diameter, aspect ratio, angle of tilt, and density of the hairs in a precise yet simple and reproducible manner.[26] In theory,[25] the adhesion strength of the manufactured artificial adhesives is given by

$$\sigma = \sqrt{\frac{8W\,E}{\pi R(1-v^2)}} \qquad\qquad (1.1)$$

where W is the work of adhesion between the two contacting surfaces, E is the elastic modulus of the material, R is the radius of the hairs, v is the Poisson's ratio of the material. Based on **Equation 1.1**, it may be concluded that the structural and material properties of pillar arrays should be optimized to improve the adhesion strength. However, there are two trade-offs in the optimization in terms of a structural design. First, a high aspect ratio of the pillar structures ensures improved adhesion but compromises the structural stability and adhesion repeatability. Second, the adhesion strength of the pillars is proportional to the elastic modulus of the polymer. However, pillar arrays made of harder materials result in lower surface adaptability, providing a significant reduction in the nanoscopic contact area. With these existing optimization strategies, it is difficult to enhance the adhesion of simple pillar patterns having flat- or round-shaped ends.

To overcome the limitations of the simple pillar shapes, many researchers focused on controlling 3D tip geometries (**Figure 1.2**).[31-35] Inspired by nature, artificial dry adhesives with various sub-micron tip structures including spatulae, mushroom (symmetric spatulae), triangular, and conical shapes have been developed.[33,36] The various tip shapes not only provide enhanced adhesion but also additional functions such as directional adhesion, suction effect, or hydrophobicity.[16,29,37,38] Among them, the mushroom-shaped (symmetric circular-shaped) tip structures were reported to have the best adhesion (**Figure 1.3**).[33,39]

A. del Campo et al. Adv. Mater. (2007)   H. Jeong et al. Proc. Natl. Acad. Sci. U.S.A. (2009)
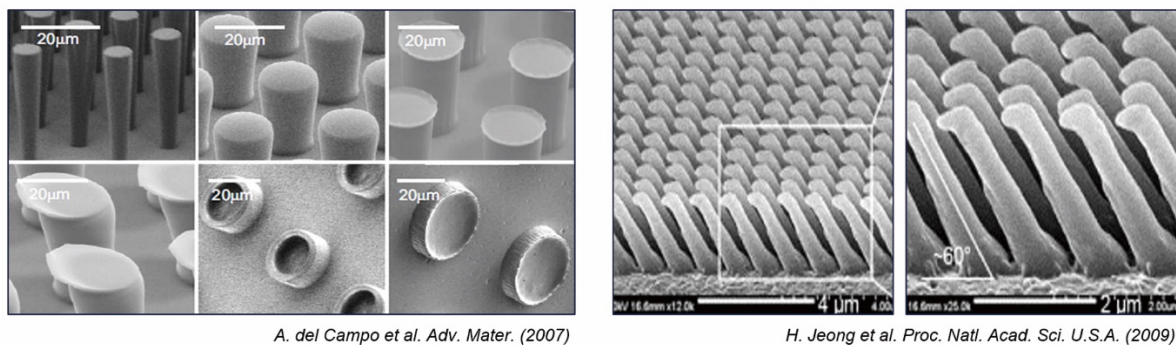
Figure 1.2. Artificial micro- and nanopillar arrays having protruding tip structures synthesized by polymeric materials. Reproduced with permission from ref.[33] © 2007 Wiley-VCH. Reproduced with permission from ref.[31] © 2009 National Academy of Sciences.

A. del Campo et al., *Langmuir* (2007)
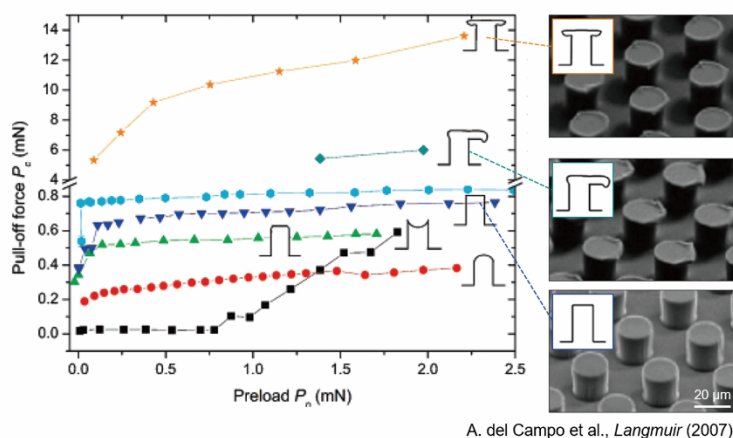
Figure 1.3. Comparison of bioinspired adhesive architectures with different tip structures. Reproduced with permission from ref.[39] © 2007 American Chemical Society.

The excellent adhesion properties of mushroom-shaped dry adhesives with protruding tips have high potential in various applications such as robotics, precision manufacturing, and biomedical devices.[5,40,41] However, previous studies on dry adhesives have used limited polymeric materials, such as polyurethane (PU), polyurethane acrylate (PUA), and polydimethylsiloxane (PDMS).[35,42] Despite the advantages of good processability, these materials limit their practical applications in advanced industries due to low thermal stability and electrical insulation.[43,44] Conventional functionalization methods such as surface coating or chemical treatment are difficult to apply since they hinder the van der Waals forces of the structures.[45,46] Although various advanced thermal and electrical fields require functional adhesives, few studies have been conducted on improving the functionality of microstructure-based dry adhesives with superior adhesion properties, such as reversible, damage-free, and clean adhesion.

1-1-3. Bioinspired Adhesives Based on 1D Nanomaterials

Over the past decades, one-dimensional (1D) nanomaterials including nanotubes, nanowires, and nanorods have been actively studied due to their unique mechanical, thermal, electrical, or optical properties.[47,48] Their excellent features originate from the extremely high aspect ratio—they have nanoscale diameters and microscale lengths (**Figure 1.4**).[49,50] Among them, carbon nanotubes (CNTs)[51,52] and silver nanowires (AgNWs)[53-55] attract the most attention of academia and industry. CNTs have superior mechanical stiffness (tensile strength of 11–63 GPa), heat resistance (thermally stable up to 2000 °C), and thermal conductivity (2800–6000 W m^{-1} K^{-1}), which are due to the hollow cylinder structure of the hexagonal carbon atom lattice. AgNWs have the best electrical conductivity (63 MS m^{-1}) among metallic nanomaterials; AgNW-based percolating networks simultaneously exhibit low sheet resistance, high optical transmittance, and high flexibility. These excellent features of CNTs and AgNWs are in high demand in advanced thermal and optoelectronic applications.

4

S.-H. Jung et al. *Appl. Sci.* (2019)   R.-Z. Li et al. *ACS Appl. Mater. Interfaces.* (2014)
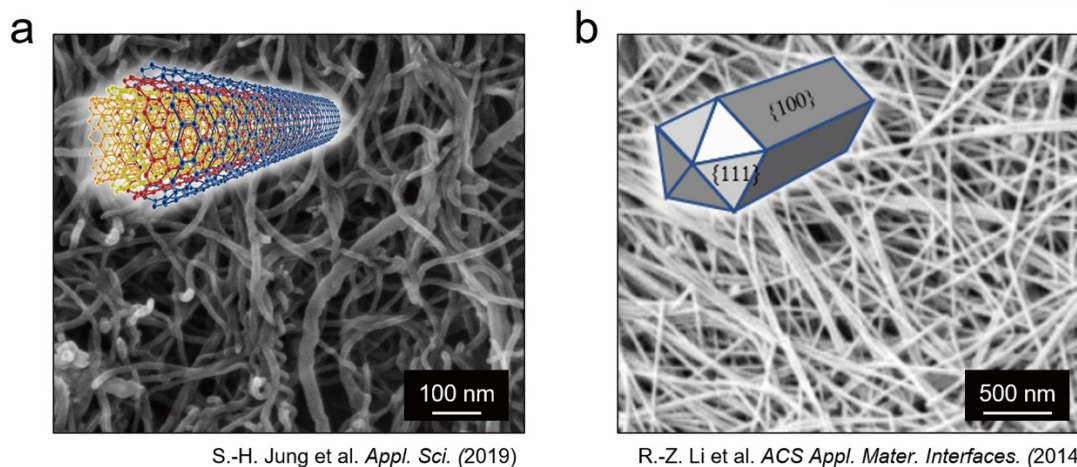
Figure 1.4. 1D nanomaterials with extremely high aspect ratio. SEM images of (a) MWCNTs (b) AgNWs. Reproduced with permission from ref.[49] © 2019 MDPI. Reproduced with permission from ref.[50] © 2014 American Chemical Society.

Excellent properties of the 1D nanomaterials can be utilized to improve the functionality of bioinspired adhesives with 3D microarchitectures. However, conventional nanomaterial-application methods such as nanocomposite molding, spray-coating, and spin-coating are not suitable for microstructure manufacturing processes. To fully demonstrate the functionality of microstructures and nanomaterials, the following must be considered. First, nanomaterials make the molding process difficult since they increase the viscosity of polymer mixtures. To address this, the concentration of nanomaterials in polymer mixtures should be optimized to satisfy the processability requirements. Second, when the nanomaterials are coated on the surface of microstructures, they hinder the intimate contacts because of their rough morphology. To solve this, nanomaterials should be selectively applied to certain areas to ensure both functionality of nanomaterials and the adhesion of microstructures at the same time. Although a variety of studies will be required to solve these problems, few studies are yet to be done to develop processes that integrate nanomaterials with bioinspired adhesive architectures.

1-2. Outline of the Dissertation

The research goal of this dissertation is to propose novel bioinspired nanocomposite adhesives with enhanced thermal or electrical properties based on the new design strategies integrating 1D nanomaterials with bioinspired 3D microarchitectures. For this purpose, we introduce new approaches for optimizing the nanomaterial composition and structural parameters of microarchitectures that enable the microarchitectures to have enhanced thermal or electrical properties while maintaining superior adhesion performance, as summarized in **Figure 1.5**.
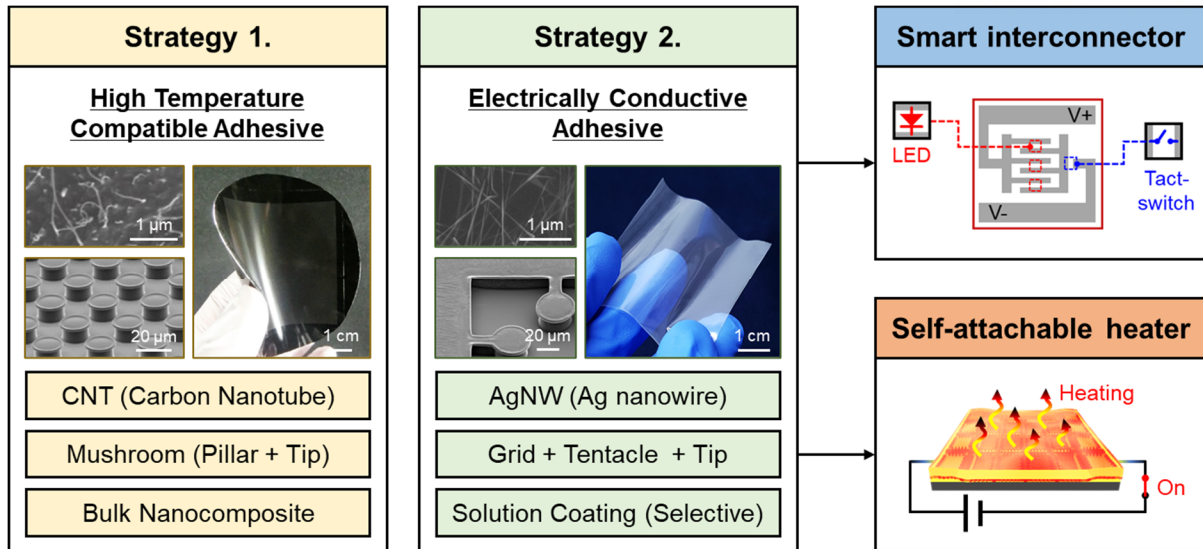
Figure 1.5. Schematic illustration of the research outline.

In **Chapter 2**, we present a high-temperature compatible adhesive based on a novel design of mushroom-shaped microarchitectures reinforced with MWCNTs of different concentrations. The MWCNT/PDMS composite adhesives exhibit remarkably better adhesion even when they are thermally annealed at temperatures up to 350 °C. We demonstrate a strong potential of bioinspired adhesives as versatile high-temperature reversible adhesives. In **Chapter 3**, we propose a flexible, transparent, and electrically conductive adhesive that is based on a distinctive design of regular grid patterns into which bioinspired adhesive architectures and percolating AgNWs are integrated. Based on the integrated design, the proposed adhesive forms reliable low-resistance electrical contacts, strong mechanical adhesive contacts, and ultra-clean contacts with active device components. The superior features of bioinspired conductive adhesives are demonstrated in smart interconnectors and self-attachable transparent heaters. Finally, in **Chapter 4**, we summarize the key achievements with suggestions for future work.

Chapter 2. High-Temperature Compatible Adhesive

2-1. Introduction

High-temperature compatible adhesives with robust adhesion strength, high reversibility, and high thermomechanical stability are essential components in various advanced applications such as flexible electronics, biochemical devices, and aerospace.[4,6,56-59] For example, commercially available polyimide tape has been widely utilized as a high-temperature protective film and interlayer dielectric due to its high thermomechanical stability.[60-63] However, chemical-based adhesive mechanisms commonly used in polyimide tape cause surface contamination by residues after separation. These inherent limitations significantly reduce the reusability of the adhesives and hinder the precise manufacturing of delicate devices. As a solution to the existing limitations, diverse bioinspired artificial adhesive surfaces based on nano- and microarchitectures were actively studied over the past decade.[5,31,37,38,42,64-70] These bioinspired adhesive architectures have demonstrated superior adhesion performance with reversible adhesion to surfaces with varying roughness and clean adhesion without causing surface contamination or damage.[29,35,64,67,70-73] Especially, hairy arrays with extruded fine tip structures provide strong, reversible, and clean adhesion in the vertical and horizontal directions.[31,69,70] The extraordinary and superior adhesion properties of the bioinspired 3D architectures enable various applications including therapeutic adhesives, grippers, and robots.[5,40,41] Despite the high interest of a variety of industries, most of the existing studies on bioinspired adhesive architectures focused on a limited number of polymers such as polydimethylsiloxane (PDMS), polyurethane (PU), and polyurethane acrylate (PUA) because of their good processability.[42] Their low thermomechanical stability and low heat resistance, however, significantly limited the application temperature range (less than 200 °C).[74] Moreover, the high-temperature adhesive behavior of polymer-based microarchitectures has not been studied sufficiently.

We developed high-temperature compatible adhesives based on a bioinspired adhesive architecture composed of multiwalled carbon nanotube (MWCNT) nanocomposites having a robust, reversible, and clean adhesion even at elevated temperatures. Multiwalled carbon nanotubes (MWCNT) were utilized as a nanofiller based on their superior thermomechanical stability. Pillars and tips of the mushroom-shaped microarchitectures were precisely manufactured by a replica-molding process with a polymeric matrix reinforced by optimized concentrations of the MWCNTs. The proposed adhesive

architectures provide excellent structural integrity, improved thermomechanical stability, and high adhesion strength even when exposed to elevated temperatures up to ~350 °C.

2-2. Results and Discussion

2-2-1. Structural Characterization of the Fabricated Nanocomposite Dry Adhesives

Figure 2.1 shows a schematic of the bioinspired composite dry adhesives with mushroom-like micropillar arrays. These arrays act as a versatile and effective form of dry adhesive as they offer strong adhesion both in the normal and shear directions without applying an external load.[5] First, a bilayer stack of the top SU-8 layer and bottom sacrificial LOR layer was formed on a Si wafer by the serial spin-coating of LOR and SU-8 on the substrate. The thickness of the LOR and SU-8 layers determines the tip thickness and pillar height of the mushroom-shaped micropillars, respectively.[69] Then, a microhole pattern was formed in the SU-8 layer. Subsequent undercut formation in the LOR layer generated a Si master with uniform negative patterns of mushroom-like micropillars (**Figure 2.2a**).
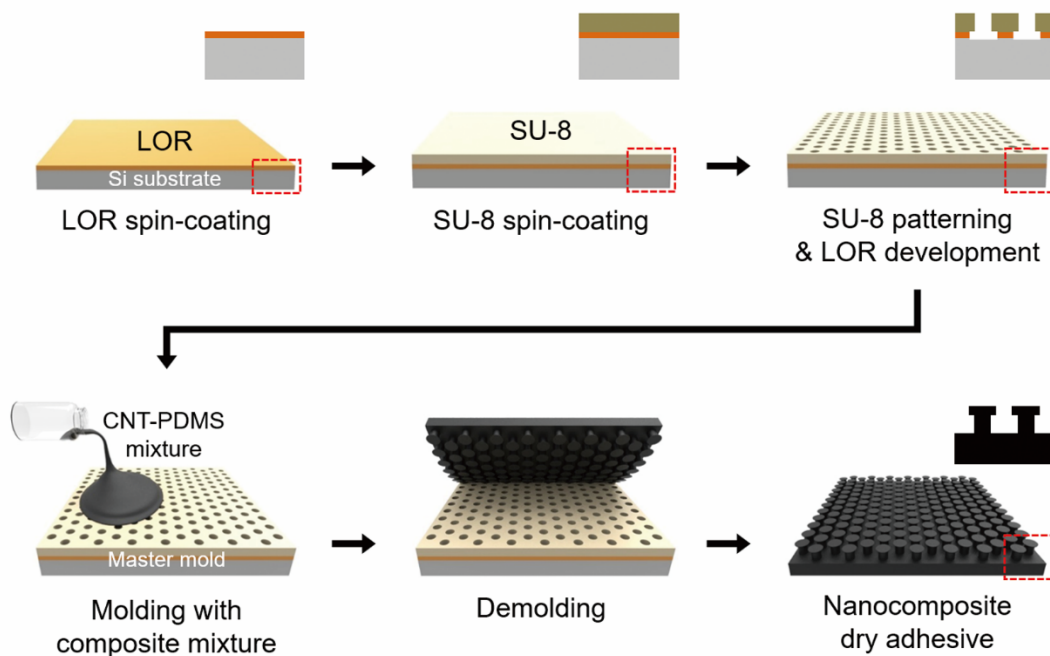
Figure 2.1. Schematic of the fabrication procedure of the nanocomposite dry adhesives with MWCNT/PDMS mixtures.
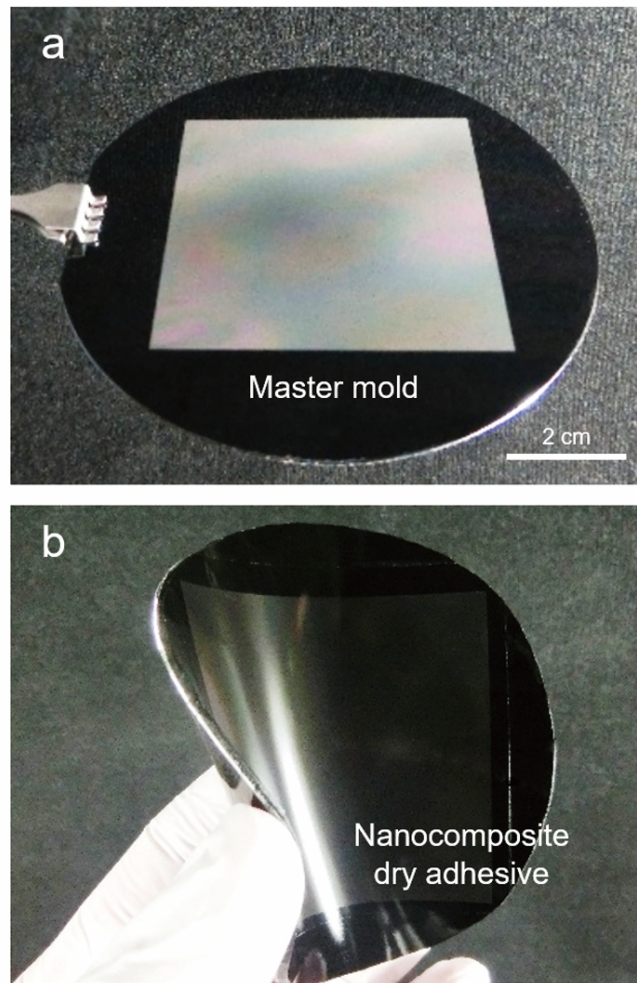
Figure 2.2. Bioinspired MWCNT/PDMS nanocomposite dry adhesives. (a) A photograph of the fabricated Si master with negative patterns of mushroom-like micropillars. (b) A photograph of the fabricated nanocomposite dry adhesives made of mixtures of PDMS and 2 wt% MWCNT.

Finally, flexible nanocomposite adhesives were obtained through the replica molding of the patterned Si master with MWCNT/PDMS mixtures containing different concentrations (wt%) of MWCNT (**Figure 2.2b**). The fabricated adhesives were cut into circular specimens for a series of tests. Nanocomposites incorporating CNT in a polymeric matrix exhibited excellent thermal and mechanical stability and high thermal conductivity, owing to the excellent physical properties and unique structures of CNT.[75,76] Thus, the fabricated nanocomposite dry adhesives are expected to have improved heat resistance and thermal-mechanical stability as compared with pure polymeric dry adhesives, and therefore, are expected to be usable at high temperatures.

Figure 2.3a shows photographs of the fabricated dry adhesives made of pristine PDMS and nanocomposites with three different concentrations of MWCNT (0.5, 1.0, and 2.0 wt%). As shown, circular dry adhesive pads with 9-mm diameter and 1-mm thickness were successfully prepared. Except for the transparent pristine PDMS adhesive, all MWCNT/PDMS composite adhesives

appeared black without any visual differences. The microstructures of all adhesive samples were investigated by scanning electron microscopy (SEM). **Figure 2.3b** shows the SEM images of the samples. Mushroom-like micropillars were successfully formed with good structural integrity and uniformity even in the sample with the highest MWCNT concentrations. The resulting micropillar arrays had a neck diameter of ~20 μm, tip diameter of ~22 μm, spacing of ~20 μm, and height of ~10 μm. The tip thickness was ~1 μm. As shown in **Figure 2.3b**, all the resulting composite dry adhesives have pillar arrays with identical geometries regardless of the MWCNT loading concentrations. Cross sections of the adhesive pads were also investigated by SEM. As shown in **Figure 2.3c**, the pristine PDMS adhesive showed a smooth cross section without any nanofiller material, whereas uniformly dispersed MWCNTs were observed in the matrix of the nanocomposite adhesives. More MWCNTs were observed in the adhesive samples with higher MWCNT loading concentrations.
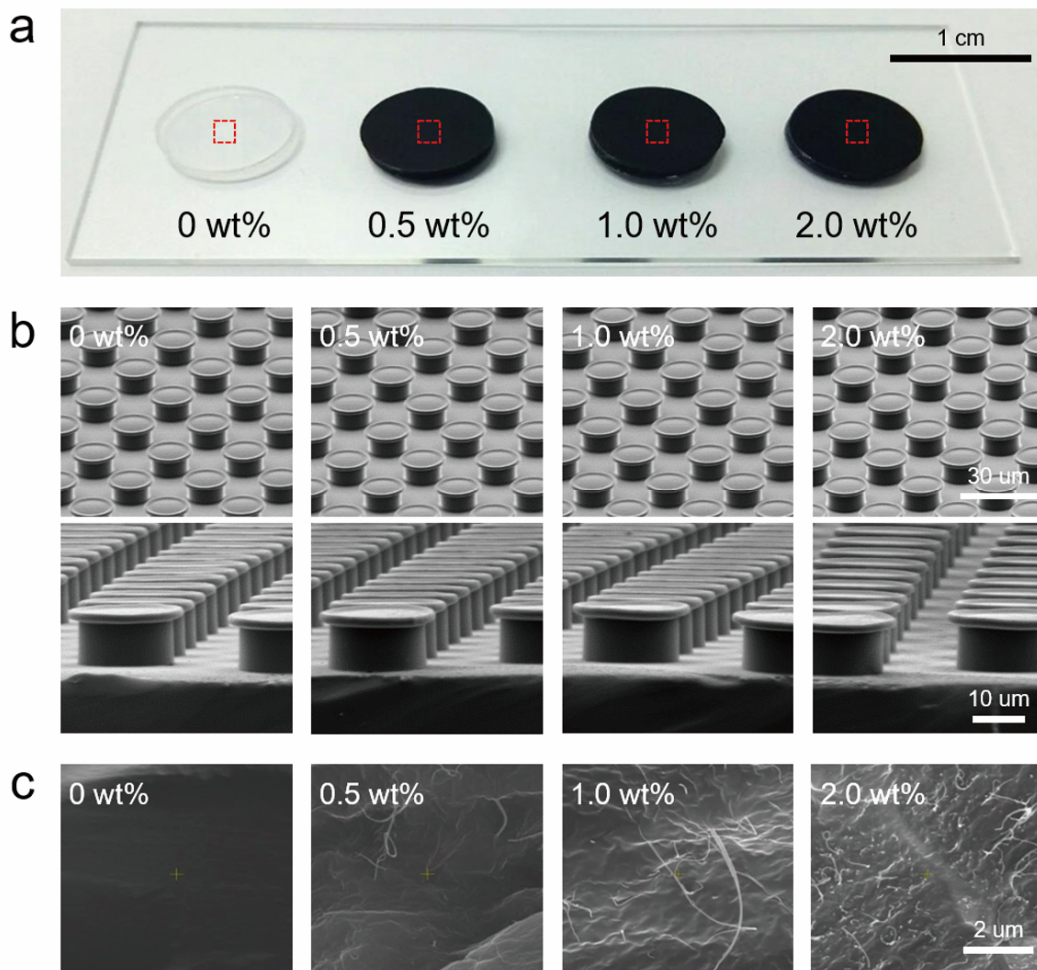
Figure 2.3. Pristine PDMS and nanocomposite dry adhesives with different MWCNT concentrations. (a) Photographs of the pristine PDMS and the nanocomposite adhesives with 0.5, 1.0, and 2.0 wt% MWCNT. (b) SEM images of the pristine PDMS and the nanocomposite adhesives with different MWCNT concentrations, corresponding to each adhesive shown in (a). (c) SEM images of the cross sections of each adhesive, corresponding to samples shown in (a)–(b).

2-2-2. Thermal Stability Analysis of the Nanocomposite Dry Adhesives

Although polymeric dry adhesives exhibit strong adhesive forces and high scalability, they can be typically used only in a limited temperature range because of the thermal degradation of polymeric materials when exposed to relatively high temperatures for a long time.[77-79] The adhesion and thermomechanical behaviors of polymeric dry adhesives at high temperatures have not been fully studied so far. To evaluate the thermal stability of the fabricated nanocomposite dry adhesives, a thermogravimetric analysis (TGA) was performed for adhesive samples with different MWCNT concentrations. To reflect the real conditions in which dry adhesives may be utilized, the TGA tests were performed in air instead of under nitrogen-purged conditions. The tendency of thermal oxidative degradation of PDMS in air is different from that in nitrogen.[43,77] **Figure 2.4** shows the resulting TGA and derivative thermogravimetric (DTG) curves of the pristine PDMS adhesive and the nanocomposite adhesives.
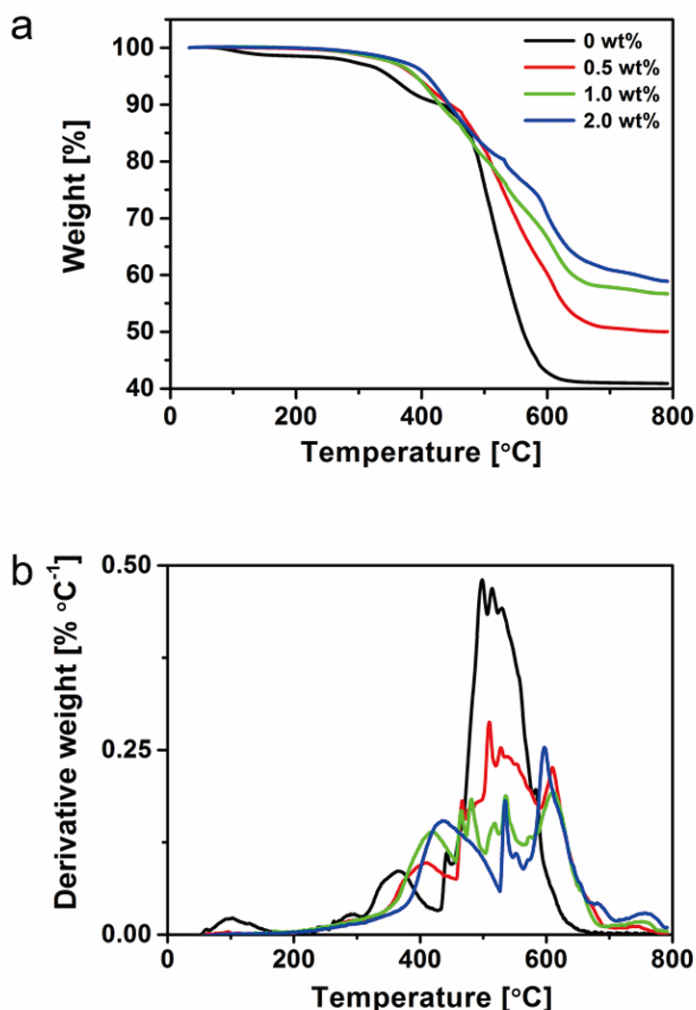
Figure 2.4. Thermal stability of bioinspired PDMS and nanocomposite dry adhesives. (a) Thermogravimetric analysis (TGA) and (b) derivative thermogravimetric (DTG) curves of the neat PDMS and nanocomposite adhesives with different concentrations of MWCNT in air.
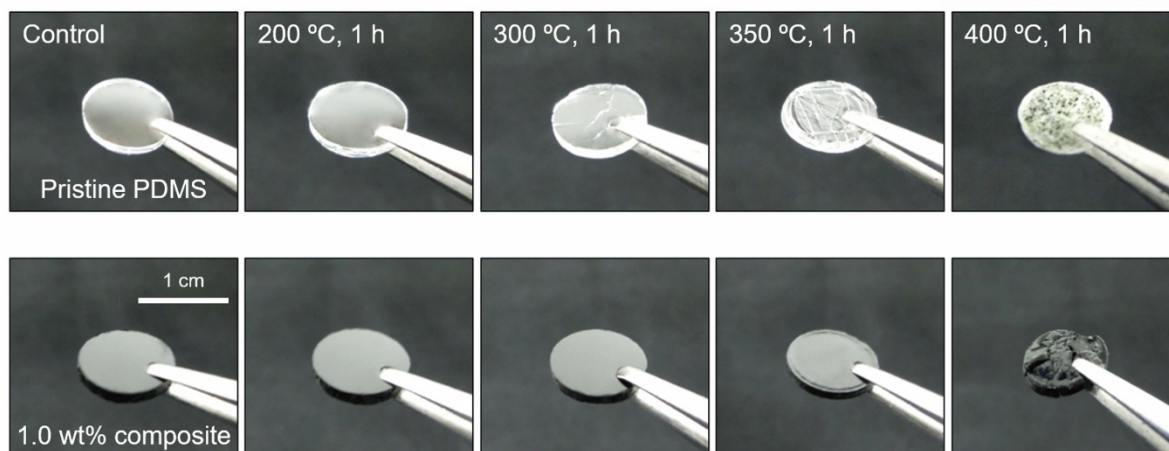
Figure 2.5. Photographs of the pristine adhesives and the nanocomposite adhesives with 1.0 wt% MWCNT after thermal annealing at high temperatures from 200 °C to 400 °C.

The thermal analysis data is summarized in **Table 2.1**. The pristine PDMS adhesive exhibited its typical thermal oxidative degradation behavior in air.[77,80] The material started losing weight at ~100 °C because of the release of the moisture absorbed on the PDMS. The temperature at the onset of decomposition and the temperature at the main decomposition peak are 300 °C and 498 °C, respectively, for the PDMS adhesive. Significant improvements in thermal stability and heat resistance were observed for the nanocomposite dry adhesives. The onset temperature increased to 348 °C and 350 °C for 0.5 and 1.0 wt% nanocomposite adhesives, respectively; the values are ~50 °C higher than the onset temperature of the pristine PDMS adhesive. The onset temperature of the nanocomposite adhesive with 2.0 wt% MWCNT was 392 °C, which is higher than that of the pristine PDMS adhesive by 92 °C. Thus, the thermal stability of the dry adhesives was drastically enhanced upon the incorporation of MWCNT into the PDMS matrix. The temperature at the main decomposition peak also greatly increased with the increase in MWCNT loading—from 498 °C for the pristine PDMS adhesive to 510, 536, and 535 °C for 0.5, 1.0, and 2.0 wt% nanocomposite adhesives, respectively. Nanocomposite adhesives with higher MWCNT concentrations showed a lower decomposition rate at the main decomposition peak (MDRT, maximum decomposition rate temperature) and a higher residual char yield (**Table 2.1**). These differences in the thermal behaviors between the pristine PDMS and the nanocomposite adhesives resulted in noticeable visual differences in the adhesives after thermal treatment. When the PDMS adhesive was cooled after thermal annealing at 100–250 °C, no visual differences were observed, as shown in **Figure 2.5**. However, after heat treatment at 300 °C and subsequent cooling, randomly oriented cracks were generated on the surface of the pristine PDMS adhesive. When the annealing temperature exceeded 350 °C, the PDMS adhesive shrunk with severe surface cracks and crumbled easily even with a low external pressure. In contrast, no surface cracks were observed up to higher annealing temperatures in the case of the nanocomposite adhesives. As shown in **Figure 2.5**, no visual differences, including surface

cracks, were observed in the nanocomposite adhesives annealed at 300 °C. Although surface expansion was observed after annealing at 350 °C, no surface cracks formed in the nanocomposite dry adhesives. The composite adhesives started shrinking and cracking upon thermal annealing beyond 400 °C. These results clearly indicate that the MWCNT/PDMS nanocomposite adhesives have remarkably improved thermomechanical stability and heat resistance as compared with those of the pristine PDMS adhesive. This is because the MWCNTs in the PDMS inhibit the mobility of the siloxane chains and interrupt the molecular rearrangement of the PDMS chain, improving the thermal stability of the MWCNT/PDMS nanocomposites.[81]

Table 2.1. Results of the TGA analysis of the pristine and nanocomposite dry adhesives with different MWCNT concentrations (0.5, 1.0, and 2.0 wt%) in air.

Specimens	Approximated onset temp. (ºC)	Temperature at the oxidation peak (ºC)	Temperature at the main decomposition peak (ºC)	Decomposition rate at the main decomposition peak (% ºC^{-1})	Residue char yield (%)
PDMS	300	364	498	0.48	40.9
0.5 wt% MWCNT /PDMS	348	410	510	0.29	50.0
1.0 wt% MWCNT /PDMS	350	419	536	0.19	56.7
2.0 wt% MWCNT /PDMS	392	435	535	0.18	58.9

2-2-3. Evaluation of Adhesion Properties of the Fabricated Nanocomposite Dry Adhesives

To investigate the effects of MWCNT concentrations and thermal annealing on the adhesion strength, the macroscopic pull-off strength was measured for dry adhesives of four different MWCNT concentrations (0, 0.5, 1.0, and 2.0 wt%) using custom-built equipment. The pristine PDMS and nanocomposites adhesives were annealed at six different bake temperatures (100, 200, 250, 300, 350, and 400 °C) for three annealing periods (30, 60, and 120 min). Then, the samples were cooled to room

temperature before measurements. In all, 76 experimental sets, including four controls, were conducted. **Figure 2.6 and 2.7** show the pull-off strength of dry adhesives with different MWCNT concentrations depending on thermal annealing conditions. The pristine PDMS adhesive without the heat treatment exhibited an adhesion strength of ~19.2 N cm^{-2} (**Figure 2.6a**). When it was baked at a slightly higher temperature of 100 °C, the changes in adhesions between samples with different annealing times were imperceptible. The average adhesion values were ~19.4, 18.4, and 20.7 N cm^{-2} after 30, 60, and 120 min of annealing, respectively. However, when the PDMS adhesive was baked at 200 °C, a notable change in adhesion strength was observed. Interestingly, the thermal treatment of the PDMS adhesive at 200 °C resulted in a significant enhancement in the pull-off strength (~27.5–29.1 N cm^{-2}) for all baking periods (30, 60, and 120 min).
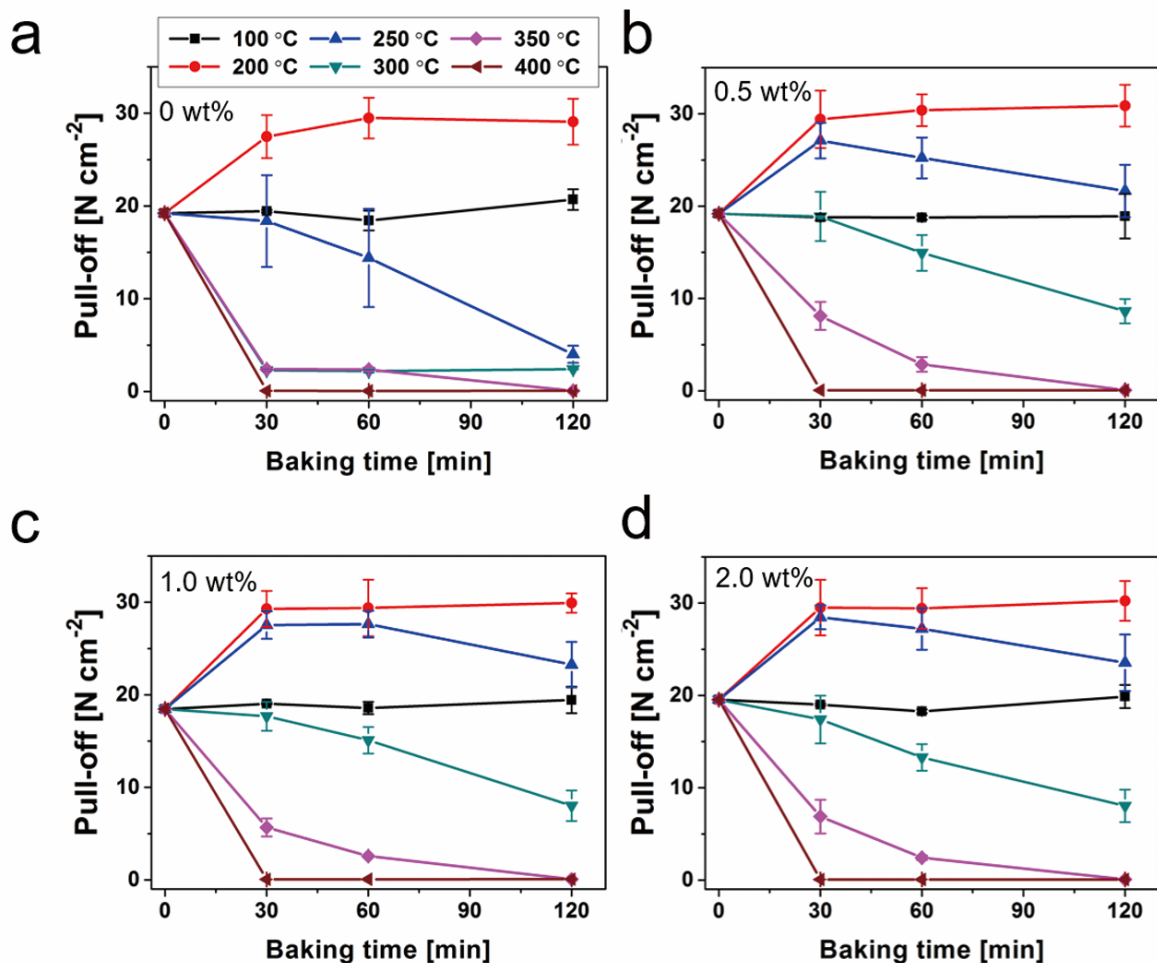
Figure 2.6. Adhesion performances of the bioinspired nanocomposite dry adhesives at room temperature after thermal annealing from 100 °C to 400 °C for different annealing times from 0 to 2 h. (a–d) Measurement of the pull-off strength of the (a) pristine PDMS dry adhesives and nanocomposite dry adhesives with MWCNT concentrations of (b) 0.5 wt%, (c) 1.0 wt%, and (d) 2.0 wt% versus thermal annealing time.
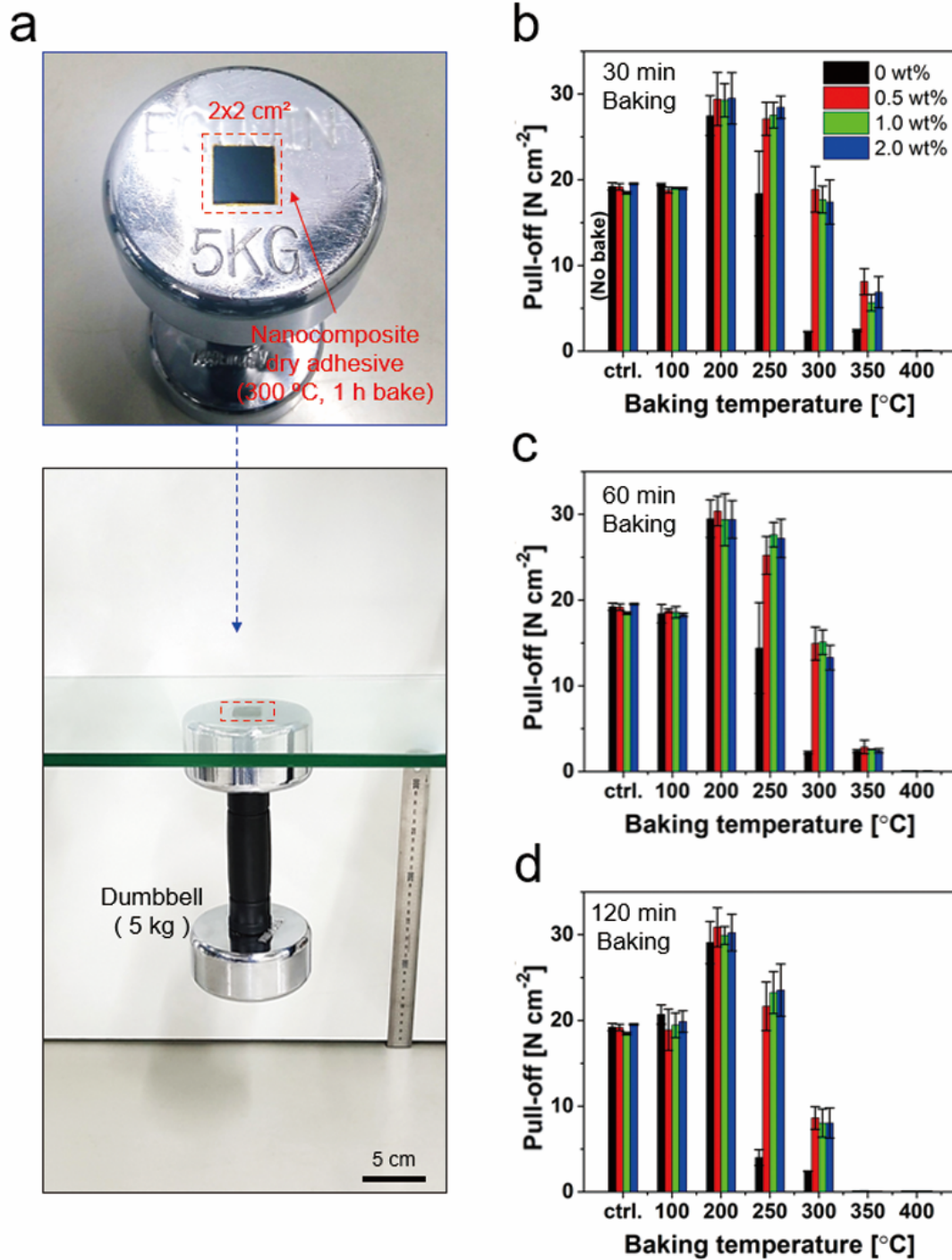
Figure 2.7. Demonstration of bioinspired nanocomposite dry adhesives at room temperature after thermal annealing from 100 °C to 400 °C for different annealing times from 0 to 2 h. (a) A photograph showing the firm attachment of a 5-kg dumbbell against a glass substrate using a nanocomposite dry adhesive (2 wt% MWCNT) that was annealed at 300 °C for 1 h. (b–d) Measured pull-off strengths of the pristine PDMS and the nanocomposite dry adhesives with different MWCNT concentrations as functions of the annealing temperature for different heat treatment times of (b) 30 min, (c) 60 min, and (d) 120 min.

15

In theory,[82,83] the pull-off force for the flat tip (P) is given by

$$P(P_p) = N(P_p)\sqrt{8\pi K R^3 W} \qquad (2.1)$$

where $N(P_p)$ is the number of pillars in contact at preload P_P, and R is the radius of the flat tip. $K = E/(1 - v^2)$ is the effective Young's modulus of the surface, and E and v are the Young's modulus and Poisson's ratio of the material, respectively. W is the work of adhesion of the interface, given as

$$W = 4 \left(\frac{\gamma_1^d \gamma_2^d}{\gamma_1^d + \gamma_2^d} + \frac{\gamma_1^p \gamma_2^p}{\gamma_1^p + \gamma_2^p} \right) \qquad (2.2)$$

where the superscripts d and p indicate the dispersion and polar components of the surface tension γ, respectively. From **Equation 2.1 and 2.2**, it can be seen that the pull-off strength can be increased by utilizing a material with higher elastic modulus and high surface tension as long as the number of micropillars in contact $N(P_P)$ remains same. The results of our contact angle (CA) tests show that the surface tension of the pristine PDMS remains almost same even after thermal treatment under different annealing conditions (**Table 2.2**). However, the elastic modulus of the PDMS increases with the annealing temperature. A previous study reported that the elastic modulus of PDMS increased from ~1.32 MPa for 25 °C to ~2.97 MPa for 200 °C annealing.[84] According to **Equation 2.1**, this ~2.25-fold increase in the elastic modulus should result in an ~1.5-fold increase in the pull-off strength, assuming Poisson's ratio of PDMS as a constant. This theoretical prediction is in good agreement with our experimental observations. The enhancement of the pull-off force for the samples after thermal treatment at 200 °C is considered induced by the resulting increase in the elastic modulus. As the elastic modulus is still relatively low (~2.97 MPa), the number of micropillars in contact can be assumed constant for the PDMS adhesive after 200 °C annealing. The pull-off strength of the PDMS dry adhesives starts decreasing significantly when baked at 250 °C. The pull-off force monotonically decreased to ~18.4 N cm^{-2} and ~14.4 N cm^{-2} after 30 min and 60 min of annealing, respectively, and was further reduced to ~4.0 N cm^{-2} after baking for 120 min; this value is only ~20 % of that of the PDMS adhesives without thermal treatment. Moreover, the pristine PDMS adhesive exhibited significantly diminished adhesion capability even after a relatively short exposure (30 min) to temperatures over 300 °C. Interestingly, this temperature corresponds to the onset temperature of pristine PDMS. As shown in **Figure 2.5 and Table 2.1**, when the PDMS is exposed to temperatures over 300 °C, thermal oxidative degradation is accelerated, and surface cracking and crumbling occurs, resulting in significantly diminished pull-off strength.

Table 2.2. Contact angles of water and glycerol on various surfaces and the calculated surface tension values by the harmonic mean method.

Specimens	Baking conditions	Contact angle (°)		Surface energy (mJ m^{-2})		
		DI water	Glycerol	γ^d	γ^p	γ
PDMS	Control	110.6 ± 1.1	98 ± 0.8	18.73	1.78	20.51
	200 °C, 1h	109.8 ± 1.3	97.6 ± 1.3	17.89	2.31	20.20
	250 °C, 1h	110.9 ± 0.5	98.8 ± 0.6	17.75	2.00	19.75
0.5 wt% MWCNT /PDMS	Control	110.7 ± 2	98.1 ± 0.9	18.74	1.75	20.49
	200 °C, 1h	109.4 ± 1.4	97.9 ± 0.3	16.55	2.90	19.45
	250 °C, 1h	110.8 ± 0.9	97.7 ± 0.6	19.77	1.41	21.18
	300 °C, 1h	105.3 ± 0.8	97.4 ± 1.6	10.82	7.01	17.83
1.0 wt% MWCNT /PDMS	Control	110.5 ± 2.5	98.3 ± 0.5	17.93	2.07	20.00
	200 °C, 1h	110.1 ± 0.4	98 ± 0.5	17.71	2.27	19.98
	250 °C, 1h	110.4 ± 2	98.4 ± 0.7	17.53	2.23	19.76
	300 °C, 1h	105 ± 0.7	97.6 ± 1.2	10.14	7.54	17.68
2.0 wt% MWCNT /PDMS	Control	110.4 ± 1.2	98.1 ± 0.3	18.12	2.04	20.16
	200 °C, 1h	110.1 ± 0.3	98.3 ± 0.1	17.13	2.47	19.60
	250 °C, 1h	110.2 ± 0.8	98.1 ± 0.5	17.72	2.24	19.96
	300 °C, 1h	104.4 ± 2.9	96.6 ± 2.7	10.75	7.41	18.16

Nanocomposite adhesives without heat treatment had pull-off strengths comparable with the strength of the PDMS adhesive (see **Figure 2.7b–d** for direct comparison). The average pull-off strengths of the nanocomposite adhesives loaded with 0.5, 1.0, and 1.5 wt% MWCNT were ~19.2, 18.5, and 19.5 N cm^{-2}, respectively. This is because the elastic modulus of MWCNT/PDMS nanocomposites with small amounts of MWCNT (0.5–2 wt%) differs only slightly from that of the pristine PDMS.[85,86] When the nanocomposite adhesives were baked at 100–200 °C, they exhibited overall adhesion tendencies similar to those of the PDMS adhesives, regardless of the loading concentrations of MWCNT. The noticeable increase in pull-off force after thermal treatment at 200 °C was also observed for all nanocomposite adhesives because of the increase in the elastic modulus after annealing at 200 °C. Overall, the effects of the MWCNT loading on the adhesion behaviors were

marginal when the adhesives were baked in a temperature range from room temperature to 200 °C. However, a noticeable difference in adhesion behaviors was observed between the PDMS and the nanocomposite adhesives for annealing temperatures over 250 °C. The nanocomposite adhesives showed high adhesion of ~27.1–28.5 N cm^{-2} after baking at 250 °C for 30 min, similar to the adhesives annealed at 200 °C. Surprisingly, the nanocomposite adhesives maintained the high level of pull-off strength even after a long baking time (~120 min). For example, the average pull-off of nanocomposite adhesives loaded with 2 wt% MWCNTs were ~28.5, 27.2, and 23.5 N cm^{-2} for 30, 60, and 120 min of annealing, respectively, at 250 °C. Although the adhesion strength decreased with the increase in baking time, the strength was still higher than that of the pristine PDMS (~19.2 N cm^{-2}) adhesive and that of the nanocomposite adhesive with 2 wt% MWCNT (~19.5 N cm^{-2}) without thermal treatments. These superior adhesion properties after high-temperature annealing were observed for all nanocomposite adhesives with different MWCNT concentrations, and their adhesion strengths were nearly identical, regardless of the MWCNT loading percentages. The nanocomposite adhesives exhibited a high level of adhesion even after annealing at 300 °C. They exhibited a pull-off strength of ~17.4–18.9 N cm^{-2} and ~13.3–15.1 N cm^{-2} for 30 min and 60 min of baking, respectively. Furthermore, the nanocomposite adhesives exhibited an adhesion of ~8.0–8.6 N cm^{-2}, which is ~41–44 % that of nanocomposite adhesives without thermal treatment, even after 120 min of baking at 300 °C. When the annealing temperature increased to 350 °C, the pull-off strength notably decreased to less than 10 N cm^{-2} as shown in **Figure 2.7**. Nonetheless, a fair adhesion of 5.7–8.1 N cm^{-2} was still observed with the nanocomposite adhesives for a relatively short annealing time of 30 min. These results demonstrate that the nanocomposite dry adhesives have superior heat resistance and thermomechanical stability, and thus can be used as a reversible and contamination-free high-temperature adhesive.

To characterize the adhesion behaviors of the nanocomposite adhesives, adhesion measurements were carried out for the different adhesives subjected to prolonged elevated temperatures without cooling. For the measurements, the adhesive and the Si substrate were placed on a hot plate, which was then heated to a target temperature. Thereafter, the adhesive and the substrate were left on the hot plate for different periods (1, 10, 20, 30, 60, and 120 min) while maintaining the temperatures. Then, the pull-off strengths of the samples were measured by bringing the dry adhesive in contact with the Si substrate. As shown in **Figure 2.8**, the pristine PDMS and the nanocomposite adhesives showed similar pull-off tendencies in the temperature range from room temperature to 200 °C. In this temperature range, both the PDMS and the nanocomposite adhesives exhibited a high adhesion strength without adhesion degradation even under prolonged continuous heating (~120 min). However, when the adhesives were heated to higher temperatures ranging from 250 °C to 300 °C, the nanocomposite adhesives showed better adhesion performance than that of the pristine PDMS adhesives. The initial pull-off strength of the pristine PDMS adhesives measured after heating to

250 °C for 1 min was ~12.9 N cm^{-2}. However, it decreased rapidly with the heating time as shown in **Figure 2.8a**. The pull-off strengths were just ~4.1 N cm^{-2} and 0.7 N cm^{-2} for 60 and 120 min of heating, respectively. In case of the nanocomposite adhesives, the initial pull-off strengths measured after 1 min of heating at 250 °C was ~13.1–14.0 N cm^{-2} depending on samples with different MWCNT concentrations. Although the adhesion decreased with heating times, the degradation rate was much smaller than that of the PDMS adhesive. Furthermore, they still exhibited high levels of adhesion even after prolonged heating for more than 1 h. The pull-off strengths after 60 and 120 min of heating were ~9.3–10.0 N cm^{-2} and ~6.4–8.1 N cm^{-2}, respectively. When the heating temperature reached 300 °C, the differences between the adhesion performances of the PDMS and the composite adhesives were more obvious. The nanocomposites exhibited a pull-off strength of more than 8 N cm^{-2} up to 20 min of heating and 2.2–4.1 N cm^{-2} even after longer heating times of 30 and 60 min. In contrast, the pristine PDMS adhesive exhibited rapidly decreasing adhesion tendencies with increasing heating times and nearly no adhesion after 30 min of heating at 300 °C (**Figure 2.8**).
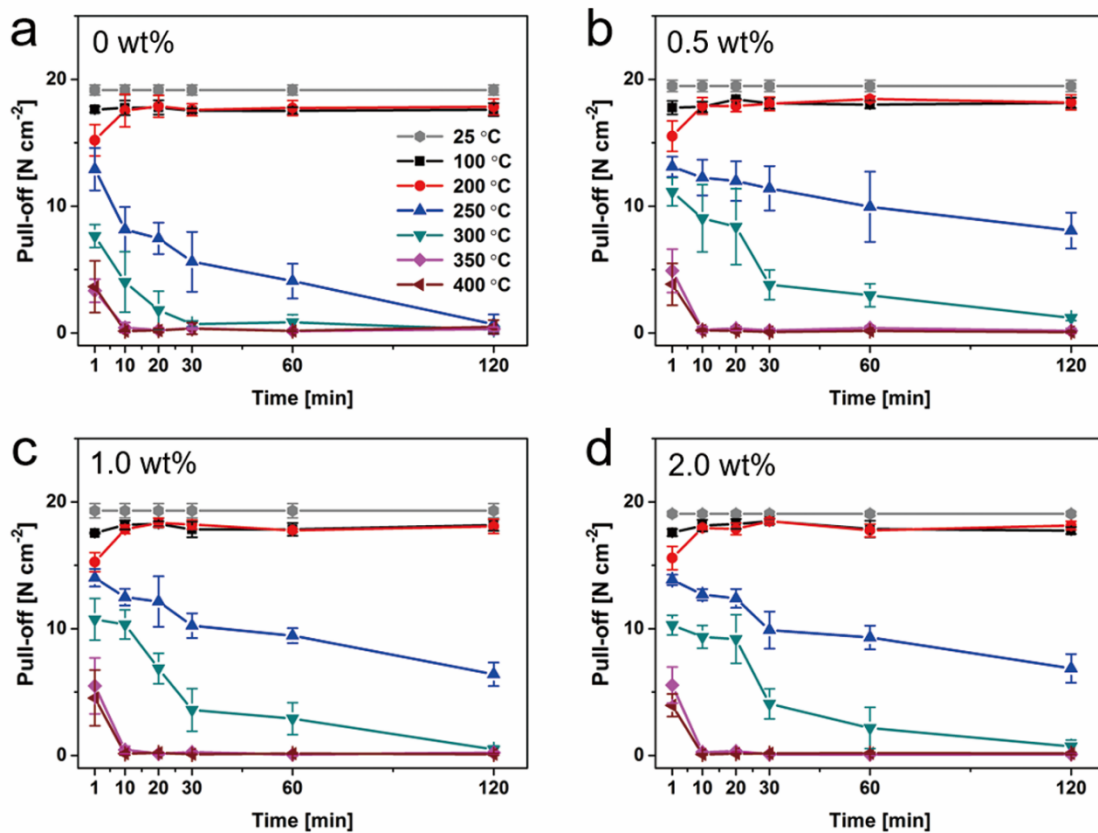
Figure 2.8. Adhesion performances of the bioinspired nanocomposite dry adhesives under prolonged elevated temperatures conditions from 25 °C to 400 °C without the cooling of the adhesives and the Si substrate. (a–d) Measured pull-off strengths of the (a) pristine PDMS dry adhesives and nanocomposite dry adhesives with MWCNT concentrations of (b) 0.5 wt%, (c) 1.0 wt%, and (d) 2.0 wt% under prolonged high-temperature conditions as a function of the heating time.

These results confirmed the superior thermal stability and high-temperature adhesion capabilities of the nanocomposite dry adhesives in comparison with pristine polymeric dry adhesives. When the heating temperature increased to 400 °C, the adhesion forces were not observed for the PDMS and the composite adhesives, except for short-term heating for 1 min. The thermomechanical stability and high-temperature adhesion performances of the bioinspired nanocomposite dry adhesives can be further enhanced by optimizing the species, sizes, and concentrations of nanofiller materials in the composites, and this will be explored in our future work.

2-3. Conclusion

In summary, we have presented a soft nanocomposite dry adhesive that can be used at high temperatures reversibly and repeatedly. The nanocomposite dry adhesives with uniform mushroom-like micropillar arrays were prepared by a simple replica-molding technique with MWCNT/PDMS mixtures over a large area of a full 4-inch wafer. The fabricated nanocomposite dry adhesives made of MWCNT/PDMS mixtures showed notably enhanced thermomechanical stability while maintaining strong pull-off adhesion even after thermal annealing–cooling cycle at high temperatures of up to 350 °C. Furthermore, they exhibited superior adhesion performances and heat resistance even under prolonged high-temperature conditions. The superior thermal stability and high-temperature adhesion capabilities of the nanocomposite dry adhesives originated from the excellent thermal and mechanical properties of MWCNT in the composite. This soft nanocomposite dry adhesive can serve as a versatile high-temperature, reversible, contamination-free adhesive for a broad range of applications—from advanced electronic devices to specialized adhesives for extreme environments.

2-4. Experimental Section

2-4-1. Preparation of MWCNT/PDMS Mixture

For the preparation of the MWCNT/PDMS mixture, multiwalled carbon nanotubes (MWCNT, CM250, Hanhwa Chemical, Korea) with diameters of 4 nm and lengths of 70–80 μm were first dispersed in chloroform by sonication (for 1 h). Then, polydimethylsiloxane (PDMS) prepolymer (Sylgard 184A, Dow Corning) was mixed with the dispersed solution at different ratios (0, 0.5, 1.0, and 2.0 wt%) of MWCNT using a magnetic stirrer. The MWCNT/PDMS mixtures were placed on a hot plate at 100 °C for 24 h to evaporate the chloroform. After the chloroform was completely evaporated, a PDMS curing agent (Sylgard 184B, 10:1 ratio by weight for the PDMS prepolymer and curing agent) was added to each MWCNT/PDMS mixture, which was then mixed by using a magnetic stirrer.

2-4-2. Fabrication of Bioinspired Composite Dry Adhesives with Mushroom-Like Micropillar Arrays

A silicon wafer was first baked at 70 °C for 10 min in a convection oven for dehydration.[69] A lift-off resist (LOR 10B, Microchem Corp, USA) was then spin-coated on the Si wafer (2000 rpm, 30 s), followed by baking on a hot plate at 200 °C for 10 min. Subsequently, a photoresist (SU-8 3010, Microchem Corp, USA) was spin-coated on the LOR layer (2000 rpm, 30 s), followed by 5-min soft baking at 100 °C. The wafer was then exposed to UV (λ = 365 nm, dose = 250 mJ cm^{-2}) light with a photomask having a microhole array. After UV exposure, the wafer was baked further at 100 °C for 3 min. Subsequently, the UV-exposed SU-8 layer was developed using an SU-8 developer (Microchem Corp, USA) for 5 min; it was then rinsed with isopropyl alcohol and blow-dried with nitrogen. The LOR layer was removed selectively with AZ 400 K (AZ Electronics Materials Corp, USA) for 60 s to form an undercut for a protruding tip of the mushroom-like micropillars. Finally, the substrate was rinsed with deionized water and blow-dried with nitrogen. For surface hydrophobization, the fabricated Si master was passivated with C_4F_8 gas. For fabricating the bioinspired composite dry adhesives with mushroom-like micropillar arrays, the prepared MWCNT/PDMS mixtures with different concentrations of MWCNT (0, 0.5, 1.0, and 2.0 wt%) were poured onto the Si master. The master covered with the mixtures was then placed in a vacuum chamber and degassed for 10 min in several tens of mTorr. Subsequently, the Si master was placed in a convection oven and cured at 70 °C for 2 h. Finally, the cured PDMS replica was carefully removed from the master.

2-4-3. Thermogravimetric Analysis (TGA)

A TGA was carried out using TGA Q500 analyzer (TA Instruments, USA) for MWCNT/PDMS composite samples with different concentrations of MWCNT. First, 15 mg of the PDMS and nanocomposite adhesives with different concentrations of MWCNT (0.5, 1.0, and 2.0 wt%) were prepared, and the samples were placed in the furnace of the analyzer. Experimental data were obtained by increasing the temperature from ambient temperature to 800 °C at a heating rate of 20 °C min^{-1} under air-purged conditions.

2-4-4. Surface Tension Characterization

To evaluate the surface tension of the PDMS and the nanocomposites after various thermal treatments, the static CAs on each planar sample were measured with a drop shape analyzer (SDLAB 200TEZD, FEMTOFAB, Korea) at room temperature by using the probing liquids deionized (DI) water and glycerol. The measurement for each liquid was repeated five times at random positions on the specimen to average the CA. The surface tension values of the PDMS and the nanocomposites

were then calculated by the harmonic mean method.

2-4-5. Pull-off Force Measurements

Macroscopic pull-off forces of the bioinspired nanocomposite dry adhesives were evaluated using custom-built equipment in a controlled temperature range 25–400 °C and a relative humidity of 40%. A circular adhesive patch (diameter = 9 mm, thickness = 2 mm) was attached to a flat Si wafer under a controlled preload of 20 N and lifted using a motorized stage at a speed of 2 mm s^{-1} until separation. For statistical significance, adhesion measurement was conducted 10 times for each sample under identical conditions.

Chapter 3. Transparent and Electrically Conductive Adhesive

3-1. Introduction

With the recent development of low-dimensional nanomaterials such as nanowires, carbon nanotubes (CNTs), and graphene, flexible and transparent conductive electrodes (FTCEs) are being developed.[87-90] In contrast to the conventional transparent electrodes based on brittle and non-flexible materials such as indium tin oxide (ITO), these nanomaterials-based electrodes exhibit high mechanical flexibility while maintaining high electrical conductivity and optical transparency.[91-95] This is owing to the superior mechanical and electrical properties of the nanomaterials. Based on the high mechanical flexibility, optical transparency, and electrical conductivity, FTCEs are key elements of the emerging flexible optoelectronic devices including flexible displays,[96] touch panels,[97,98] heaters,[99,100] solar cells,[101-103] electronic skins,[104-106] and smart windows.[107]

In these flexible devices, the FTCEs should form a close, intimate mechanical contact and adhesion with various active components of the flexible devices to ensure stable, low-resistant electrical contacts.[108] Flexible optoelectronic devices rely on the stable and intimate electrical and mechanical contacts between electrodes and active device components.[109] Unstable contact formations at the interfaces of the electrodes and active device components can cause malfunctions and performance degradation of electronics and efficiency reduction of energy devices, adversely affecting device reliability.[7,110] However, FTCEs based on percolating nanomaterial network typically cannot adhere to other surfaces with its nanomaterials-coated side as the coated nanomaterials hinder the conformal contact of the FTCEs with the substrates.[46,111] Thus, additional contact formation steps are necessary for the conventional FTCEs. Conventional contact formation methods include the use of soldering,[112] conductive adhesives,[7] or mechanical clamper.[113] Alternatively, conductive metal electrodes can be formed directly on the specific active regions of flexible devices using vacuum evaporation[114] or solution coating.[115] While these approaches for forming mechanical and electrical junctions are well-established, they have several limitations. For example, it is challenging to form an accurate, thin contact with soldering because of the viscous fluid nature of the solder paste.[112] Moreover, solder pastes are not transparent, which limits their utilization in specific regions of flexible transparent

devices.[112] The mechanical fixation using a sprung metal clip is typically bulky and is not suitable for thin, flexible devices. In addition, the mechanical clamping can damage the surface physically.[113] Fixations using conductive tapes and pastes (e.g., Ag paste) generally contaminate the surface and increase contact resistance owing to the adhesive chemicals at the contacting interfaces.[7] Metal deposition can damage the active layer of devices and also requires expensive vacuum processes.[114] Solution coating of conducting nanomaterials on a semi-finished device is also challenging owing to the solvent compatibility and solvent-induced damage.[115] Notwithstanding extensive researches into flexible transparent electrodes, FTCEs that can simultaneously form low-resistant electrical contacts and strong mechanical adhesive contacts with damage-free, clean contact interfaces, and junctions have rarely been explored.

Herein, we report a self-attachable, flexible, transparent, and conductive electrode (AF-TCE) that can simultaneously form strong mechanical adhesive contacts and low-resistant electrical contacts with diverse planar and curvilinear surfaces of flexible devices. The AF-TCE has a distinctive design of regular grid patterns into which bioinspired adhesive architectures and percolating silver nanowires (AgNWs) are integrated. Based on the integrated design, the AF-TCE can form low-resistant electrical ohmic contacts and ultra-clean, damage-free contact interfaces with active components of flexible devices by attaching it onto the components even when they are highly bent. Moreover, specific electronic circuits can be formed on the surface of the AF-TCE by depositing AgNWs selectively. This enables interconnections among the diverse electronic components on its surface. The advantages of the proposed AF-TCE are demonstrated by utilizing it for flexible electronics.

3-2. Results and Discussion

3-2-1. Design of the Self-Attachable, Flexible, Transparent Conductive Electrode

Figure 3.1 shows a conceptual schematic of the AF-TCE proposed in this study. The AF-TCE consisted of four main device components: the grid pattern, tentacles, extruded tips, and selectively-deposited percolating AgNWs (**Figure 3.1a, b**). The grid pattern functions as the main framework of the AF-TCE (**Figure 3.1a**). It enables the precise control of the optical and electrical properties of the AF-TCE. However, the grid pattern cannot exhibit an adequate adhesion to substrates or active components of flexible devices. To achieve this, we integrated adhesive architectures available in nature into the grid pattern (**Figure 3.1b, c**). Nature has developed diverse adhesion mechanisms based on unique structures.[15-21] For example, *Drosera* (sundews) has tentacles with glandular heads that cover the leaf surface (**Figure 3.1c**).[116,117] The long hairy tentacles provide structural flexibility and increase the contact area with objects, which facilitate the capture of insects. Geckos also have hierarchical hairs with protruding tips (**Figure 3.1c**), which provide strong dry adhesion by

24

maximizing van der Waals interaction.[24,69,118] Among the many unique features of gecko foot hairs, the protruding tips play critical roles in maximizing the adhesion strength by uniformly distributing stress at the contact interfaces. Structures similar to the tentacle structures of *Drosera* and the tip structures of gecko foot hairs were harnessed in our design of the AF-TCE with the objective of forming robust electrical and mechanical adhesive contacts with various active components of flexible devices (**Figure 3.1d**). The AgNW networks that are selectively deposited on the grid pattern provide conductive percolating paths across the entire surface of the AF-TCE (**Figure 3.1b, d**).
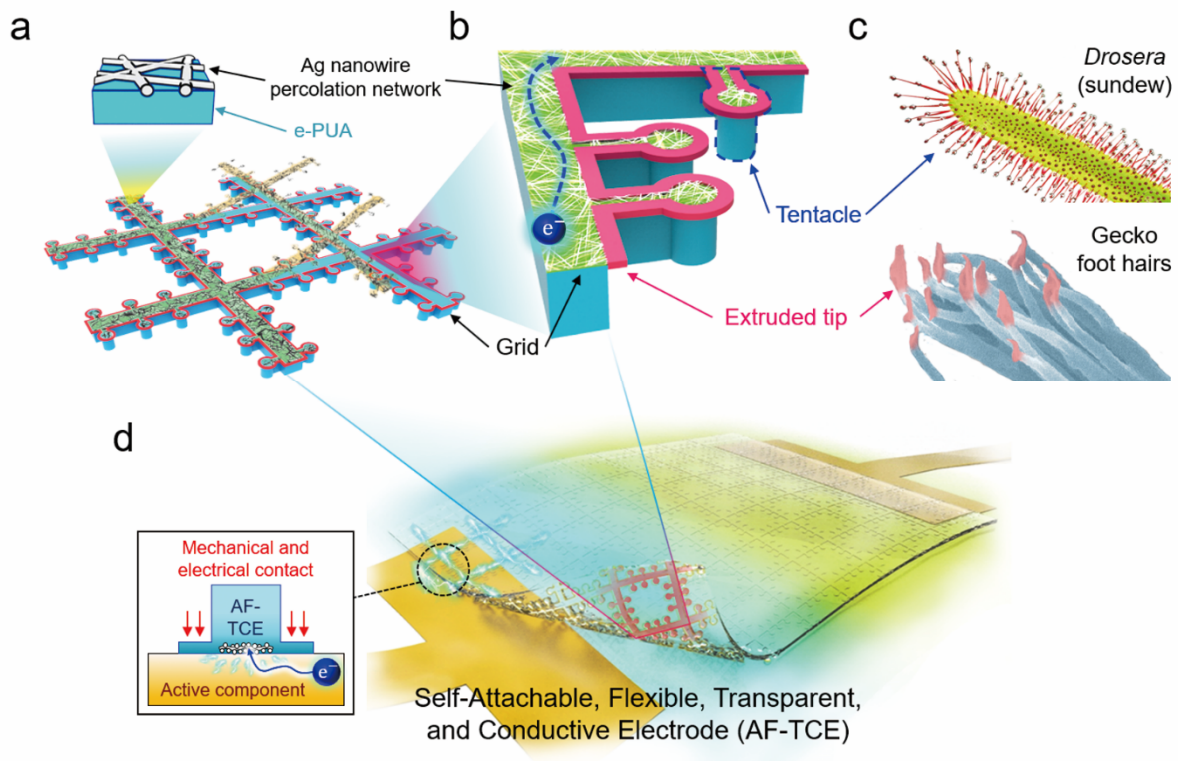
Figure 3.1. Design of self-attachable flexible transparent conductive electrode. (a) Schematic illustration showing grid structure with bioinspired adhesive structures of AF-TCE, on which AgNW percolating networks are deposited selectively, (b) conceptual schematic showing an enlarged view of the structure of AF-TCE. The tentacles and protruding tips are generated along with the regular grid patterns, whereas the AgNWs are deposited along the grid. (c) structures of sundew (top) and gecko foot hairs (bottom), (d) a conceptual illustration showing the AF-TCE that conformably attach to active components of flexible devices. The inset shows a cross-section of AF-TCE in contact with active device components.

The AF-TCE was developed by the replica molding of a Si master having a negative grid pattern, with an ultraviolet (UV)-curable polymer (**Figure 3.2**). Briefly, negative patterns of grids with

tentacles and protruding tips were prepared on a Si wafer by photolithography using a bilayer of photoresist (PR) and lift-off resist (LOR). An AgNW solution was then deposited in the trench of grid patterns. Replica molding of the patterned Si master with the UV-curable elastic polyurethane acrylate (e-PUA) added with a plasticizer (Triton) yielded the AF-TCE. Instead of using e-PUA and AgNWs, other materials can be used for fabricating the AF-TCE. For example, stretchable polymers such as polydimethylsiloxane, Ecoflex, and hydrogel, can be used for the matrix.[119-122] Carbon-based nanomaterials such as CNTs and graphene can be utilized for the conductive networks.[88,123]
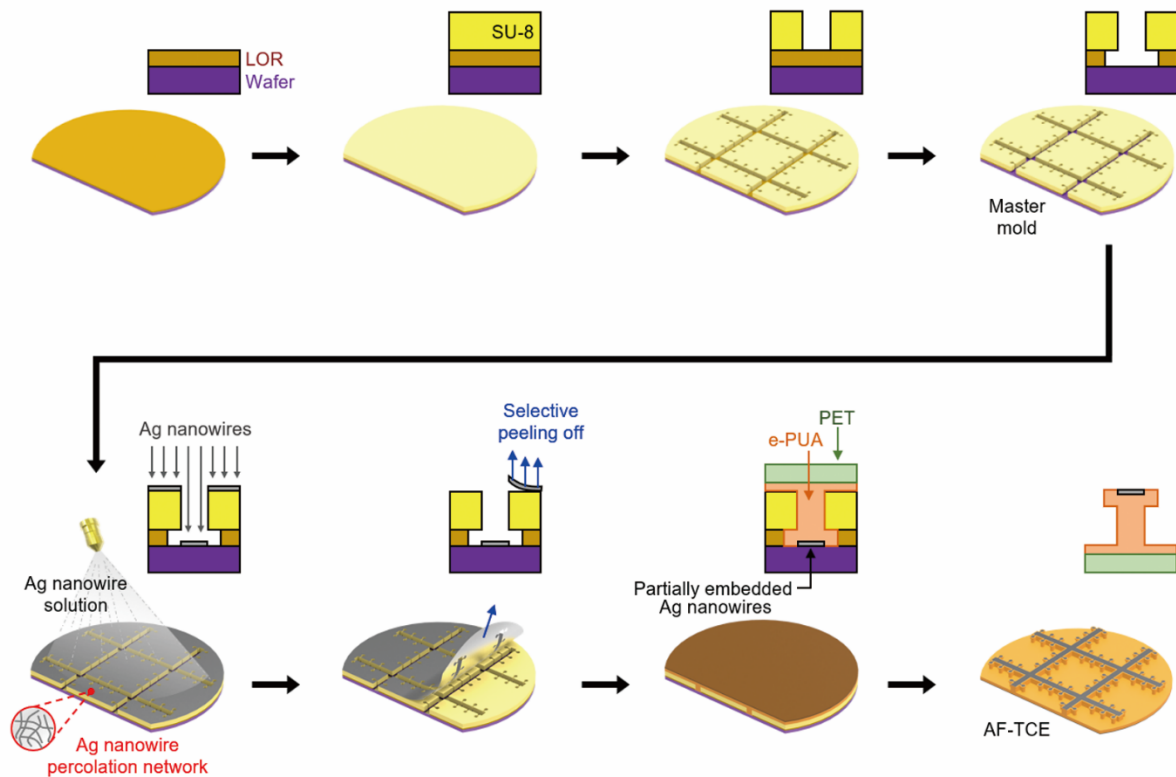
Figure 3.2. Schematic of fabrication process of self-attachable, flexible, transparent, and conductive electrode.

The resulting AF-TCE resembles a highly flexible and transparent thin film (**Figure 3.3a, b**). Microscopically, tentacle structures were generated on each side of the grid (**Figure 3.3c, d**). The grid was 40 µm in width, 10 µm in height, and 400 µm in center-to-center pitch (**Figure 3.4)**. The tentacle size was 30 µm in head diameter, 5 µm in stalk width, 55 µm in total length, and 40 µm in pitch. In addition, the grid and tentacle have protruding tips (**Figure 3.3e**) with an extruded length and thickness of 3 µm and 2 µm, respectively. With the tentacle and tip-integrated grid structures, the AF-TCE could achieve strong and intimate adhesion to diverse planar and non-planar surfaces without using additional adhesives (**Figure 3.3b**).
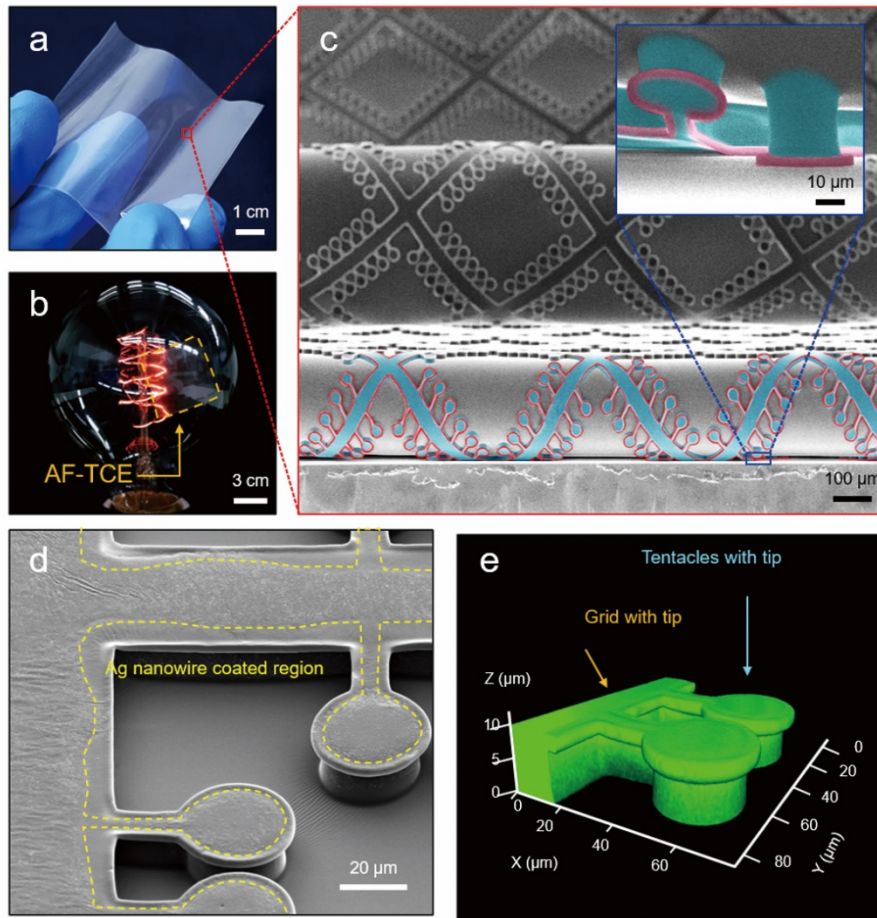
Figure 3.3. Structures of AF-TCE. (a) Image of the fabricated AF-TCE, (b) image of AF-TCE that is intimately attached to curved surface of a light bulb, and (c) SEM images of the fabricated AF-TCE. The inset shows that the grid with tentacles and tips is firmly adhered to the bottom substrate. (d) SEM image showing the AgNW-coated AF-TCE, (e) 3D confocal microscopy image showing grid structure integrated with tentacles and tips.
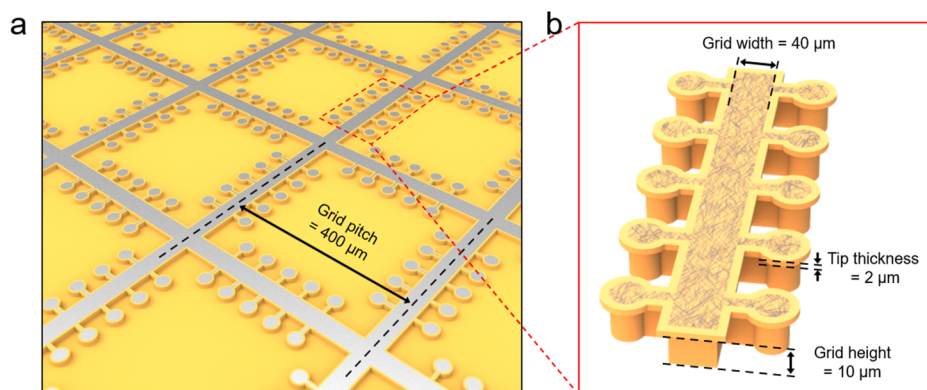
Figure 3.4. Schematic of the detailed geometrical parameters of AF-TCE. (a) Grid structure with bioinspired tentacle structures with the protruding tips of AF-TCE, on which AgNW percolating networks are selectively deposited. (b) Enlarged view of a grid line of AF-TCE.

The scanning electron microscopy (SEM) analysis results shown in **Figure 3.5a** reveal that AgNWs with an average diameter of 20 nm and length of 20 μm were deposited uniformly over the grid and tentacle structures, forming percolating conductive networks. Note that the AgNWs were not coated on both the sides (i.e., tip region) of the grids and tentacles to enable a strong self-adhesion of the AF-TCE (**Figure 3.5a-i**). When the contacting surface of the tip is covered with AgNWs, its adhesion performance could be deteriorated significantly.[124] Furthermore, energy dispersive spectroscopy (EDS) analyses verified that AgNW percolating networks were selectively deposited along the grid and tentacles, without depositions on the wing tip region (**Figure 3.5b**).
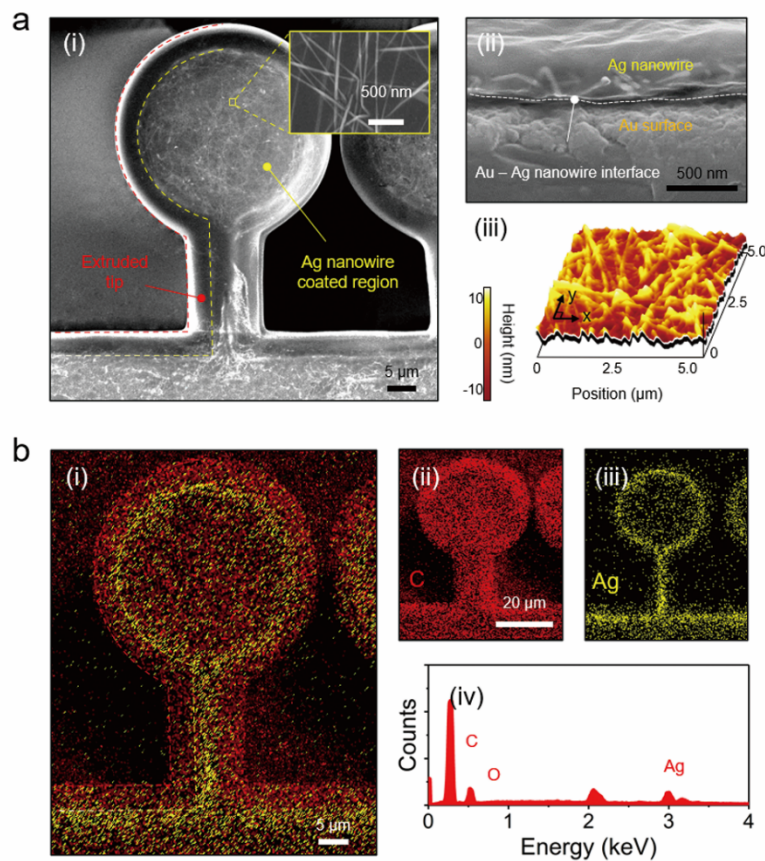
Figure 3.5. Surface topography of AF-TCE (a) (i) SEM image showing AgNWs that are selectively deposited along the grid and tentacle of AF-TCE. The inset shows an enlarged SEM image of AgNW coated region. (ii) SEM image showing a cross-section of AF-TCE in contact with an Au coated PET substrate, (iii) AFM images of AgNW networks that are partially embedded in the underlying e-PUA matrix. (b) EDS mapping analysis of AgNWs coated over the AF-TCE. (i) Merged image of carbon (C) and silver (Ag) elements of AF-TCE. (ii) C and (iii) Ag elements that are observed over surfaces. (iv) EDS spectrum collected from top surface of AF-TCE.

In general, AgNWs coated on flexible substrates are delaminated from the substrates owing to the low adhesion between the nanowires and substrates.[111,125] In our case, the AgNWs were partially

embedded in the e-PUA after the replica molding process, as depicted by the SEM and atomic force microscopy (AFM) images (**Figure 3.5a-ii, iii**). Therefore, the AgNWs were not delaminated from the surface of the AF-TCE even when the electrode was highly bent while the partially exposed side of the nanowires could function as conductive pathways. Conductive composites, which typically consist of polymeric matrix and conductive fillers, can be utilized for obtaining improved mechanical stability under high deformation conditions.[123] However, they have limited optical transparency. Based on the coordinated, integrated structures of the grid, tentacle, tips, and AgNWs, we anticipated that the resulting AF-TCE can provide a general strategy to form damage-free, robust, and controllable contact interfaces to diverse active layers of flexible devices. Recent studies have demonstrated that transferrable top electrodes can form damage-free contact interfaces with junction quality similar to that by vacuum-based electrode deposition.[126] In addition, they enable the decoupling of the fabrication process of the top electrode from the remaining device fabrication process. This simplifies the production process of flexible devices substantially.

3-2-2. Mechanical Adhesion and Contact Behaviors of AF-TCE

To investigate the effect of tentacle and tip structures on the adhesion of the AF-TCE, the adhesion strengths were evaluated for three types of electrodes: a grid electrode (G), grid electrode with tentacles (GT), and grid electrode with tentacles and tips (GTT) (**Figure 3.6**). We conducted finite element analysis (FEA) to compare the adhesive behaviors of the three different electrodes (G, GT, and GTT) in contact with a flat Si substrate when separation occurs. During the separation, the G and GT electrodes showed stress concentrations around the grid edges, which could result in low adhesion strengths.[25] However, the GTT electrode withstood much higher stresses until it was separated from the substrate as the tip structures could uniformly distribute the stress at the contact interface. These results showed that the adhesion strengths of the AF-TCE could be enhanced not only by the increased contact area but also by the uniform stress distribution (**Figure 3.7**).
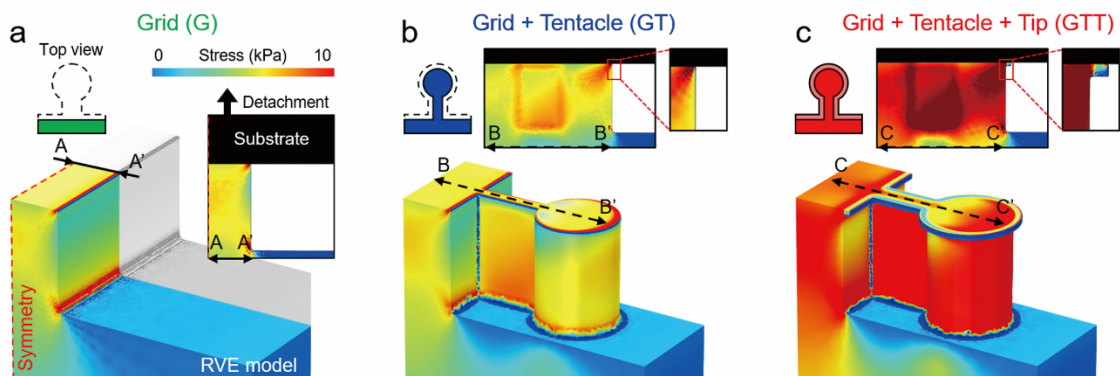
Figure 3.6. FEA simulations of adhesive behaviors of (a) grid (G), (b) grid with tentacles (GT), and (c) grid with tentacles and tips (GTT) structures in contact with a flat Si substrate when separation occurs.
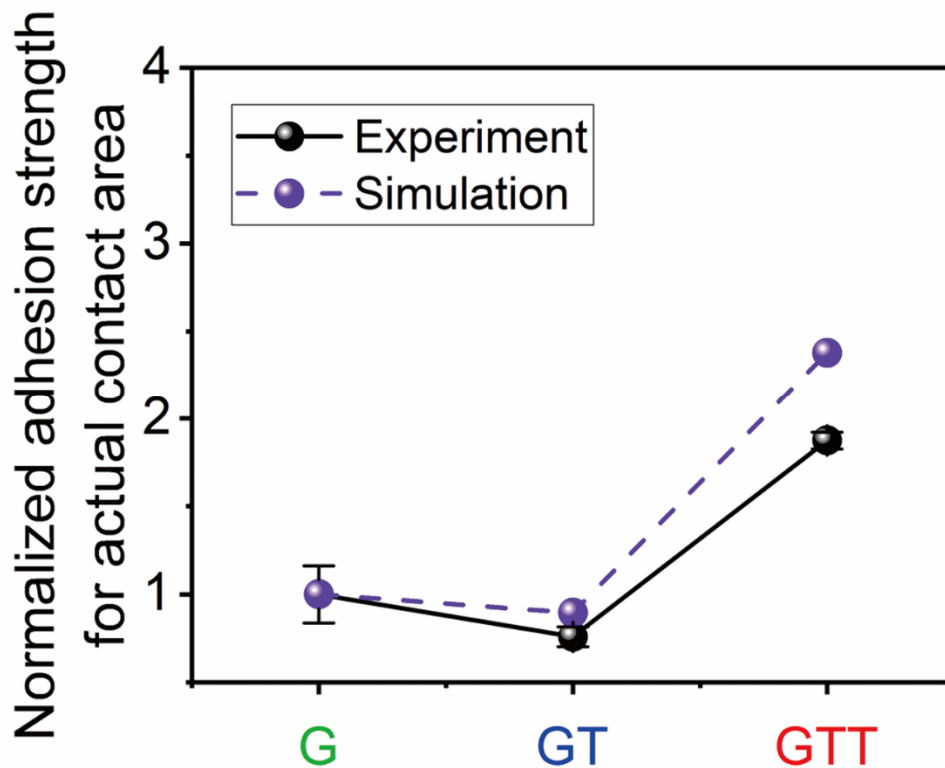
Figure 3.7. Normalized adhesion strengths of G, GT, and GTT structures (the measured adhesion strengths of each structure with respect to that of the G structure, P/P_G) against a flat Si substrate. Adhesion strengths were calculated based on the actual contact area of each structure.

The self-attachable property of the AF-TCE was evaluated by measuring the adhesion strengths of the AF-TCE on a flat Si substrate (pulling rate: 1 mm s^{-1}). **Figure 3.8a** shows the measured adhesion strengths of the different electrodes without coatings of AgNWs. With a preload of 80 kPa, the GT electrode showed a higher adhesion strength (151.7 kPa) than that of the G electrode (120.6 kPa) as the tentacle structure increased the contact interfaces with the substrate. A grid electrode with tips (GTP electrode) also exhibited an enhanced adhesion strength (221.5 kPa) compared to that of the G electrode owing to the uniform stress distribution by the tip structure. Interestingly, the GTT electrode exhibited a significantly higher adhesion of 477.2 kPa even compared to those of the G, GT, and GTP electrodes. This is because the GTT structure enabled the simultaneous utilization of the uniform stress distribution effect by the tip structure and the increased contact area effect by the tentacle structure. The GTT electrode displayed higher adhesion strengths (177.7 kPa) compared to the G (2.6 kPa) and GT (23.5 kPa) electrodes even when AgNWs were selectively deposited over the electrodes (preload: 80 kPa, AgNW dosage: 111.1 μg cm^{-2}) (**Figure 3.8b**). The adhesion strength of the GTT electrode with AgNW coatings was enhanced further with an increase in the preload and attained 382.8 kPa under a preload of 2,000 kPa. In contrast to the GTT electrode, the G and GT electrodes have saturated adhesion with a preload of over ~400 kPa.
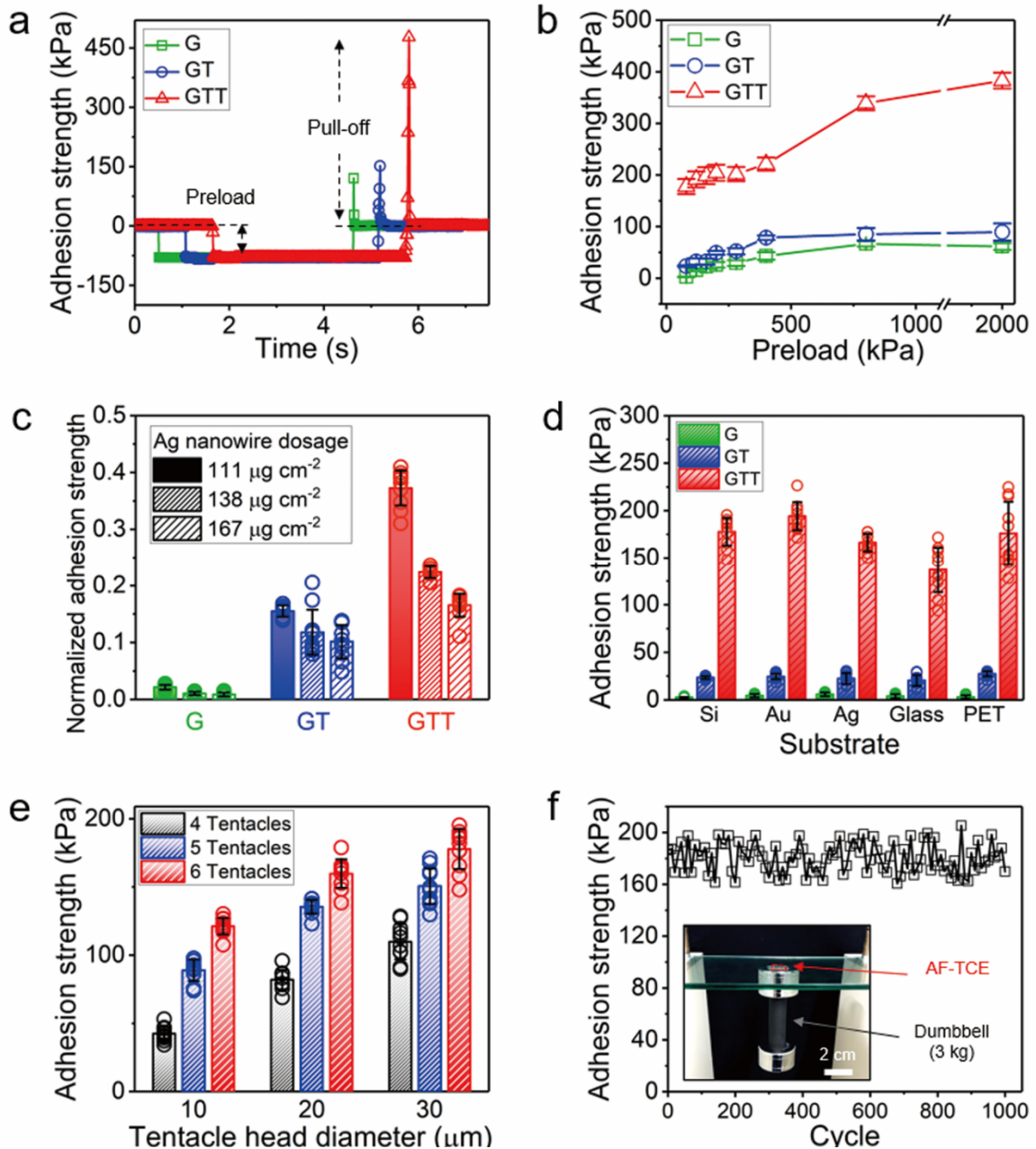
Figure 3.8. Mechanical adhesion and contact behavior of the AF-TCE. (a) Representative examples of measured adhesion strengths of G, GT, and GTT structures against a Si substrate under preload of 80 kPa. The retraction speed was 1 mm s^{-1}. (b) Adhesion strengths of G, GT, and GTT structures as a function of preload. (c) Normalized adhesion strengths of G, GT, and GTT structures as a function of coating dose of AgNWs. (d) Adhesion strengths of G, GT, and GTT structures against different substrates. (e) Adhesion strengths of G, GT, and GTT structures with different numbers and head sizes of tentacles. (f) Adhesion repeatability and durability of AF-TCE during repeated cycles of attachment and detachment. The inset is an image that shows a 3 kg dumbbell attached firmly to a glass substrate through the AF-TCE (area: 1.5×1.5 cm^2).

We also examined the effect of the amount of deposited AgNWs on the adhesion strength for a fixed preload of 80 kPa (**Figure 3.8c**). Higher amounts of AgNWs can result in higher conductivity of the AF-TCE. However, the adhesion strength of the AF-TCE was reduced with an increase in the amount of AgNWs. This indicates the necessity of optimizing the AgNWs to ensure a balance between the self-attachability and conductivity of the AF-TCE. Nonetheless, the GTT electrode could maintain a relatively high adhesion strength even after the deposition of AgNWs. The normalized adhesion strength (defined as the measured adhesion strength of AgNW-deposited electrode with respect to that of the electrode without AgNWs) of the GTT electrode was in the range of 0.165 to 0.373 depending on the AgNW dose. In contrast, the normalized adhesion strength of the G electrode was negligible (0.009–0.022). These results verify that the distinctive design of the GTT electrode integrated with the bioinspired adhesive architectures plays a significant role in equipping the electrode with robust self-adhesion capability.

In addition to the Si substrate, the GTT electrode also exhibited remarkably higher adhesion strengths for a wide range of substrates including Au, Ag, Glass, and PET, (polyethylene terephthalate) compared to those of the G and GT electrodes (**Figure 3.8d**). The strong self-attachability of the GTT electrode to diverse metallic, semiconducting, and polymeric substrates would enable versatile applications of the electrode in diverse flexible devices. The adhesion strength of the GTT electrode was dependent on the number and size of the tentacle structures (**Figure 3.8e**). With an increase in the number of the tentacle at each side of the unit grid and in the diameter of the tentacle, the adhesion strength increased owing to the increased contact area with the substrate. Based on the strong adhesion property, the AF-TCE could firmly adhere to diverse substrates as well as hold significant weight with high repeatability (**Figure 3.8f**).

3-2-3. Electrical and Optical Behaviors of AF-TCE

Flexible transparent electrodes require high electrical conductivity and optical transparency.[127] **Figure 3.9** shows the optical and electrical properties of the AF-TCE with a grid filling factor ($f = w / s$, where w and s represent the width and spacing of the grid, respectively) of 0.1. Depending on the filling factor and the amount of coated AgNWs, the transmittance (T) and sheet resistance (R_s) of the AF-TCE could be modulated in the range of 35–90 % (at 550 nm) and 5×10^0–1×10^5 Ω sq^{-1} (**Figure 3.10**). For example, for an R_s of 100 Ω sq^{-1}, the transmittance of the AF-TCE could be 81.8 % for a grid with f of 0.1. For an R_s of 10 Ω sq^{-1}, the transmittance of the AF-TCE could be 76.4 % for a grid with f of 0.1 (**Figure 3.9**).
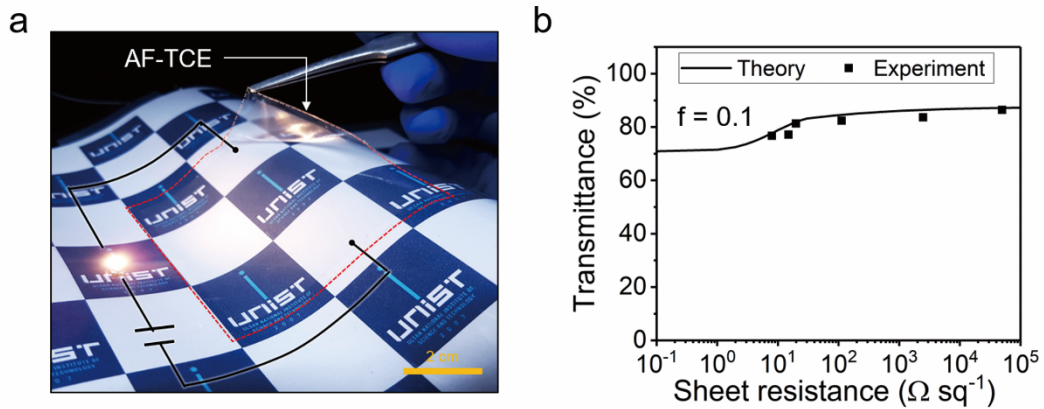
Figure 3.9. Electrical and optical behavior of AF-TCE. (a) Photograph showing that the AF-TCE is attached to a curved surface with robust mechanical and electrical contacts. (b) Sheet resistance versus transmittance at 550 nm for AF-TCE with a filling factor of 0.1.
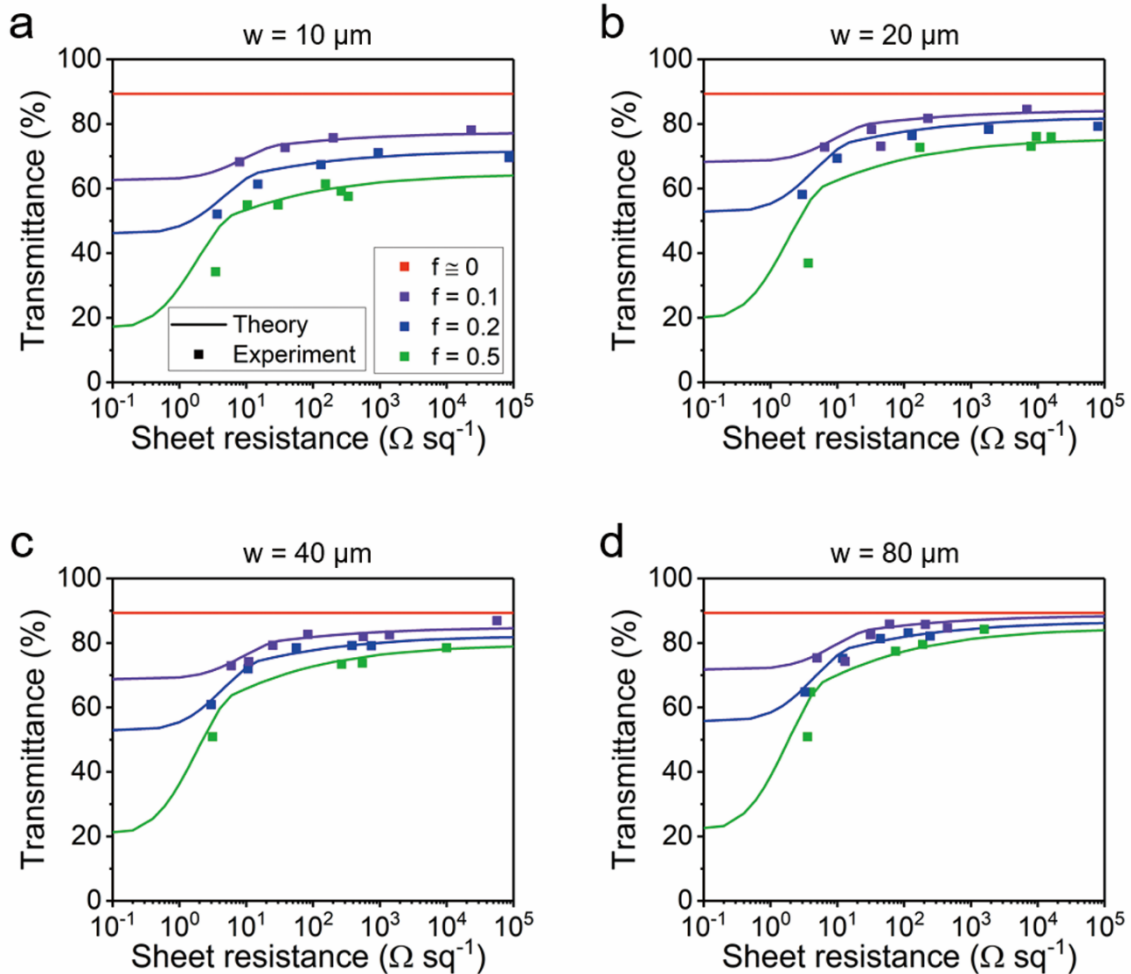
Figure 3.10. Theoretical curve and experimental data of electrical and optical behavior of AF-TCE. (a–d) Sheet resistance versus transmittance at 550 nm with different filling factors (f = ~0, 0.1, 0.2, 0.5) and with different grid widths (w) of (a) 10 μm, (b) 20 μm, (c) 40 μm, (d) 80 μm.

When the filling factor (*f*) and a coating layer of the AgNWs are considered in conjunction, the transmittance of the AF-TCE can be expressed as

$$T = T_i\big[1 + f(f-2)\big(1 - T_{film}/100\big)\big] \qquad (3.1)$$

where T_i is the transmittance of the uncoated grid and T_{film} is the film transmittance of the AgNW-coated film. Based on the percolation theory,[128] T_{film} is expressed as

$$T_{film} = \left\{1 + \frac{Z_0\sigma_{op}}{2}\left(\frac{t_c^{\,n}}{\sigma_{DC,B}R_s}\right)^{1/(n+1)}\right\}^{-2} \qquad (3.2)$$

where Z_0 is the characteristic impedance of the free space (377 Ω), σ_{op} is the optical conductivity (6.5×10^3 S m^{-1}), t_c is the critical thickness (160 nm), n is the percolation exponent, and $\sigma_{DC,B}$ is the bulk DC conductivity of the AgNW-coated film (2.7×10^6 S m^{-1}). Note that $n = 0$ for a relatively low R_s. Herein, the AgNW-coated film behaves similar to bulk ($R_s < \sigma_{DC,B}^{-1} t_c^{-1}$). Meanwhile, $n = 1.9$ for $R_s \geq \sigma_{DC,B}^{-1} t_c^{-1}$. This implies that the film behaviors are in the percolation regime. Applying **Equation 3.2** into **Equation 3.1** yields

$$T = T_i\left[1 + f(f-2)\left\{1 - \frac{1}{100}\left(1 + \frac{Z_0\sigma_{op}}{2}\left(\frac{t_c^{\,n}}{\sigma_{DC,B}R_s}\right)^{1/(n+1)}\right)^{-2}\right\}\right] \qquad (3.3)$$

The experimental results were in good agreement with the theoretical predictions (**Figure 3.9, 10**).

For a grid with *f* of 0.1, the *T*, R_S, and adhesion strength (P_{ad}) of the AF-TCE were evaluated as a function of the AgNW dose (**Figure 3.11**). Without AgNW coating, the AF-TCE exhibited a *T* of 87.6 % and P_{ad} of 477 kPa without displaying electrical conductivity. When the AgNW dose increased to 111.1 μg cm^{-2}, *T*, R_S, and P_{ad} were 81.3 %, 20 Ω sq^{-1}, and 177.7 kPa, respectively. For an AgNW dose of 166.7 μg cm^{-2}, *T*, R_S, and P_{ad} were 76.7 %, 8 Ω sq^{-1}, and 78.9 kPa, respectively. Different ranges of *T* and R_S values are required for transparent conductive electrodes depending on the applications: *T* > 90% and R_S < 10 Ω sq^{-1} for solar cells,[127] *T* > 80 % and R_S < 20 Ω sq^{-1} for OLED,[129] *T* > 60 % and R_S < 700 Ω sq^{-1} for touch panel,[129] and *T* > 60% and R_S < 100 Ω sq^{-1} for heater.[130] Tunable *T* between 35 % and 90 % and R_S between 5×10^0 Ω sq^{-1} and 1×10^5 Ω sq^{-1} were achieved for the AF-TCE by controlling the *f* values and coating amounts of the AgNWs. Furthermore, the adhesion strength of the AF-TCE could be modulated between 79 and 477 kPa, which is higher than those for previous dry adhesives (3–340 kPa).[131,132] Therefore, the AF-TCE with adjustable *T*, R_S, and P_{ad} in the practical performance ranges can be utilized for diverse flexible optoelectronic and energy devices.
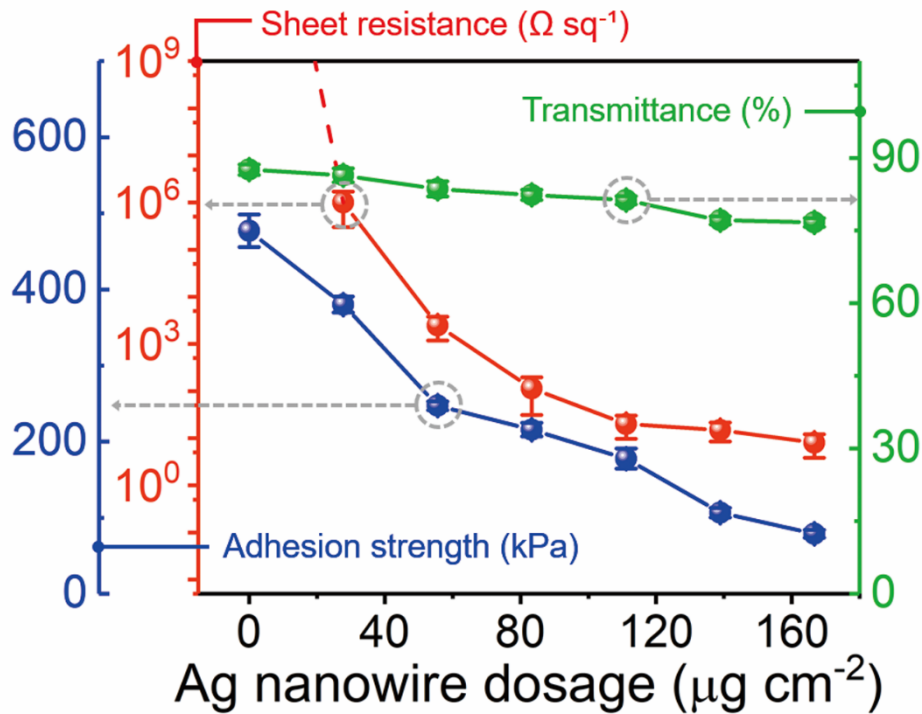
Figure 3.11. Sheet resistance, transmittance, and adhesion strength of AF-TCE ($f = 0.1$) as a function of coating dose of AgNWs.

Next, we investigated the current–voltage characteristics of the AF-TCE in contact with different metallic (Au, Ag, and Ti) and semiconducting (p-type Si) substrates (**Figure 3.12a**). The AF-TCE was placed on the substrates with a low preload of 0.1 kPa. Note that the preload was removed during the current–voltage measurement. Linear current–voltage curves were observed on the metallic substrates, indicating that the AF-TCE could form highly effective ohmic contacts with the metallic substrates with a low preload without using conductive adhesive pastes, vacuum deposition process, or high-pressure application. The AF-TCE formed a rectifying, Schottky contact with the p-type Si substrate, as typically observed at metal–semiconductor interfaces. **Figure 3.12b** shows the current–voltage relationships of the AF-TCE in contact with Au substrate under different preloads ranging from 0.1 to 60 kPa. When the preload increased from 0.1 kPa to 5 kPa, the measured resistance was reduced. This indicated that a more intimate electrical junction was formed at the electrode–Au interface owing to the application of the higher preload. However, preloads above 5 kPa did not induce a noticeable decrease in the resistance. This shows that the AF-TCE could form a robust ohmic contact even under a low preload of 5 kPa without requiring the application of high pressure for forming the intimate mechanical contact. For the p-type Si substrate, significant variations in the current–voltage curves were not observed regardless of the level of preload (**Figure 3.12c**). This verifies that the AF-TCE can form intimate and strong mechanical adhesive contacts and robust electrical contacts with diverse metallic and semiconducting substrates with a low preload.

35
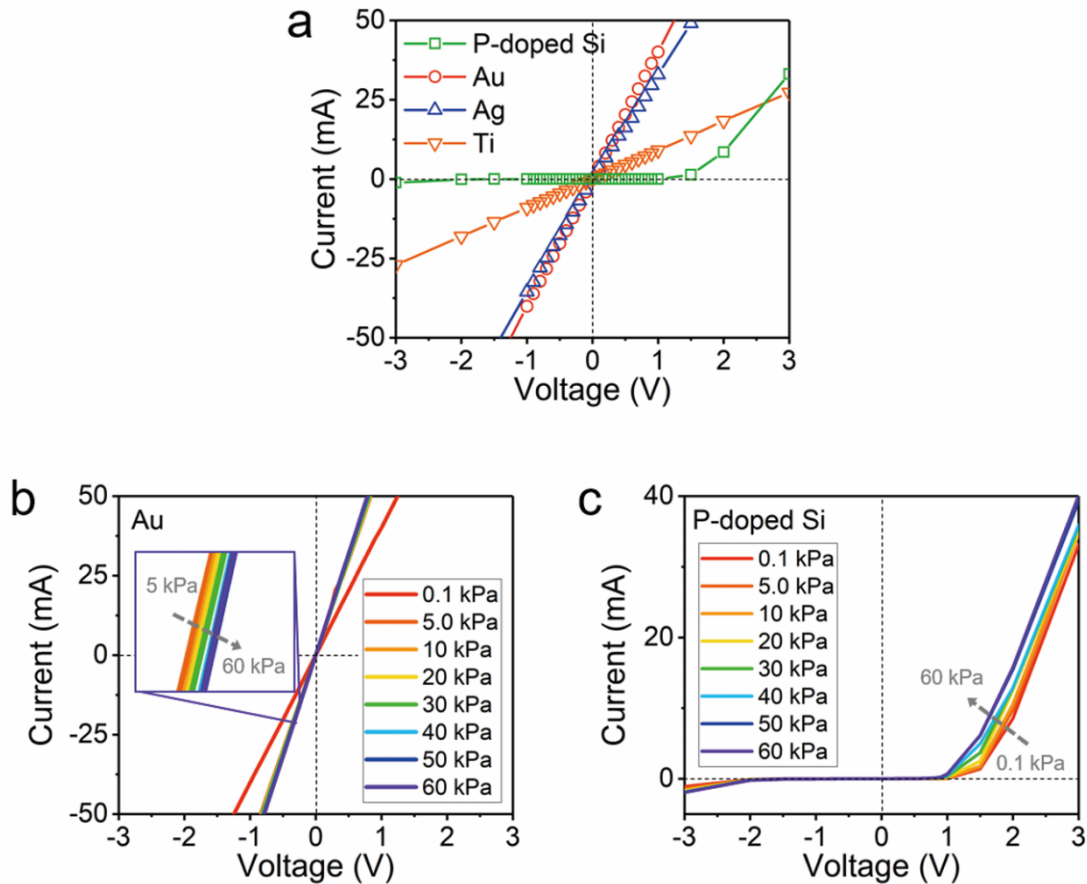
Figure 3.12. Electrical contact behavior of AF-TCE (a) Current–voltage characteristics of AF-TCE in contact with different metallic and semiconducting substrates. (b, c) Current–voltage behavior of AF-TCE in contact with an (b) Au and (c) p-type Si substrate for different preloads.

The contact resistance at the Au–AF-TCE interface was evaluated as functions of the coating amount of AgNWs and preload (**Figure 3.13, 14**). The contact resistance was reduced with an increase in the preload. In particular, the contact resistance exhibited significantly reduced and saturated values with a preload of 10 kPa. Higher preloads did not induce a noticeable further decrease in the contact resistance. Under a low preload (< 0.1 kPa), AF-TCEs with higher doses of AgNWs showed higher contact resistance than those with lower doses of AgNWs. This is because the surface coated with more AgNWs has higher surface roughness and therefore, has smaller contact interfaces with the substrate (**Figure 3.5a-iii**).[133] With a higher preload, the AF-TCE coated with more AgNWs could form intimate contacts with the substrate and displayed lower contact resistance than the AF-TCE deposited with a lower amount of AgNWs. The contact resistance of 40 kΩ μm could be obtained with the AF-TCE with a preload above 10 kPa (**Figure 3.13**). This is comparable to the reported contact resistance values in the previous reports.[134]
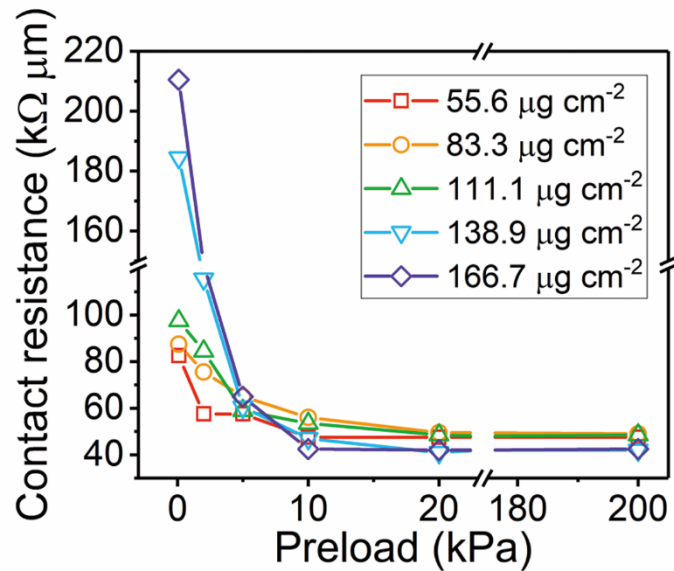
Figure 3.13. Contact resistance of AF-TCE coated with different doses of AgNWs as a function of preload.
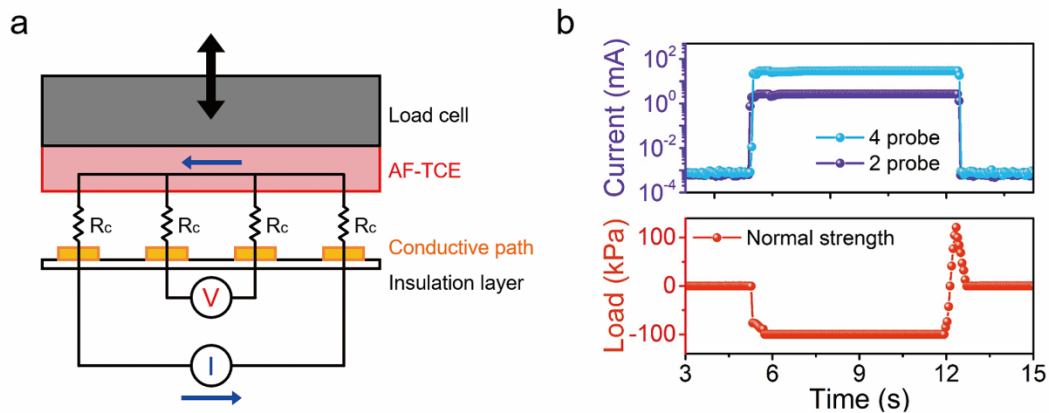
Figure 3.14. Experimental set-up for measuring contact resistance of AF-TCE (a) Schematic of experimental set-up for four-point probe-based contact resistance measurement. b) Representative examples of measured current (two-probe contact and four-probe contact) and adhesion strength of AF-TCE (R_s = 20 Ω sq^{-1}).

3-2-4. Applications of AF-TCE to Flexible Electronics

To demonstrate the application of the AF-TCE as a transparent, self-attachable electrode and interconnector with ultra-clean, thin interfaces in flexible devices, we used it to connect light-emitting diodes (LEDs) on flat and curved substrates. To achieve this, AgNWs were selectively deposited over the grid of AF-TCE to form a circuit of separated, repeating conducting paths for the application of bias voltage to individual LEDs (**Figure 3.15**). The AF-TCE was optically transparent (**Figure 3.16a**). When a blue LED was placed on the AF-TCE, the LED turned on immediately (**Figure 3.16a-ii, iii**). A simple placement of the blue LEDs on the surface of the AF-TCE yielded a robust mechanical

attachment and electrical connection of the LEDs. The connected blue LEDs could be simply disconnected from the AF-TCE without any visible residue on the AF-TCE (**Figure 3.16a-iv**). After detaching the blue-LEDs, white LEDs could be readily connected to the AF-TCE (**Figure 3.16a-v, vi**). The AF-TCE enabled the repeatable electrical connections of multi-color LEDs that represented a variety of alphabetic arrangements (A-F-T-C-E), without the use of non-transparent and messy conducting adhesive pastes, bulky mechanical sockets, or complicated wired connection (**Figure 3.16b**).
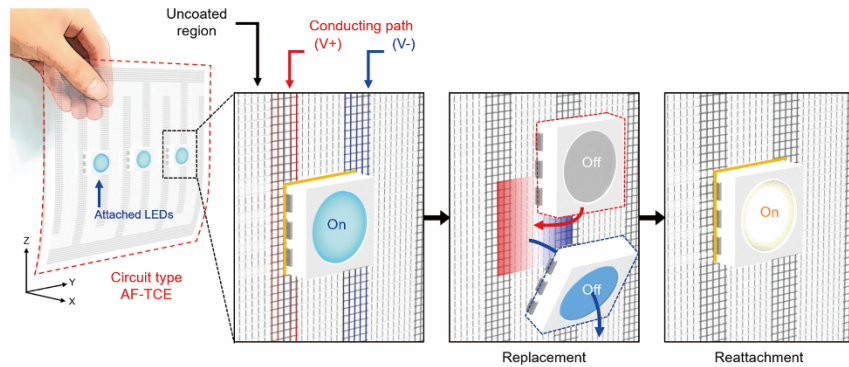
Figure 3.15. Conceptual illustration showing reversible interconnection of LEDs using AF-TCE with AgNW-based circuits.
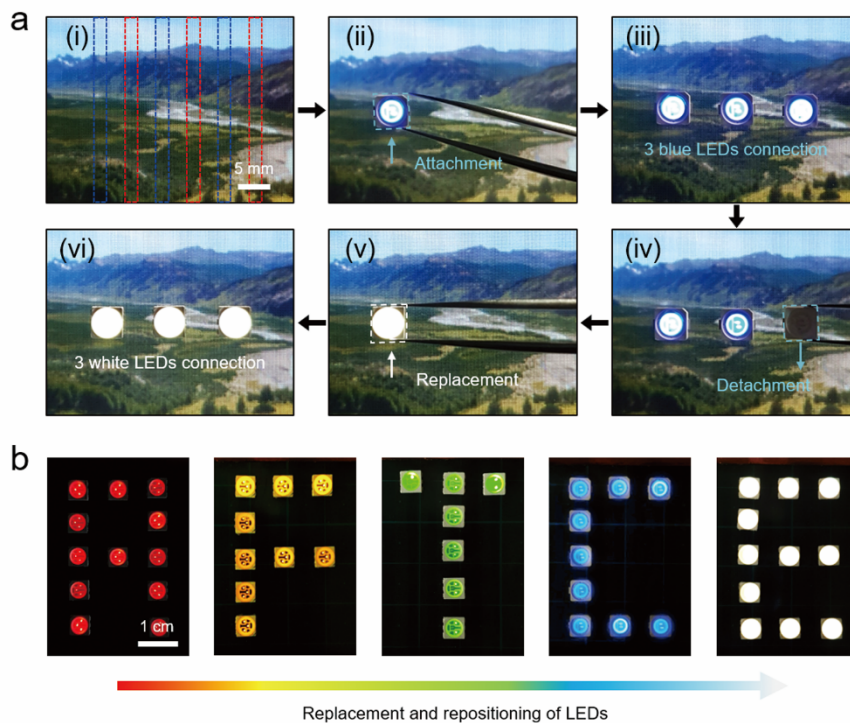
Figure 3.16. Application of AF-TCE as smart interconnector. (a) Images showing the demonstration of the reversible interconnection of LEDs. (b) Images showing the replacement and repositioning of LEDs with different colors, generating different alphabetic arrangements of "A-F-T-C-E."

38

The AF-TCE was also highly flexible and therefore could be conformably applied to curved substrates (**Figure 3.17**). Even when the AF-TCE was highly bent, the LEDs could be connected firmly to curved AF-TCEs. An advantage of the AF-TCE is that specific electronic circuits can be formed on the surface of the AF-TCE by selectively depositing AgNWs, thereby enabling interconnections of diverse electronic components on its surface. **Figure 3.18** shows a simple exemplary circuit that can connect LEDs and switches. As illustrated, LEDs and a tact switch could be interconnected on the curved AF-TCE and operated normally. Meanwhile, each side of the AF-TCE could be attached firmly to the vertical and horizontal glass substrates.
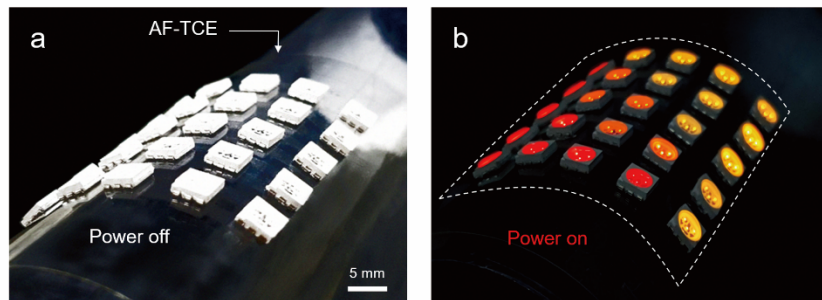
Figure 3.17. AF-TCE smart interconnector applied to curved surface. Images showing LEDs conformably attached to a curved AF-TCE with (a) power-off and (b) power-on.
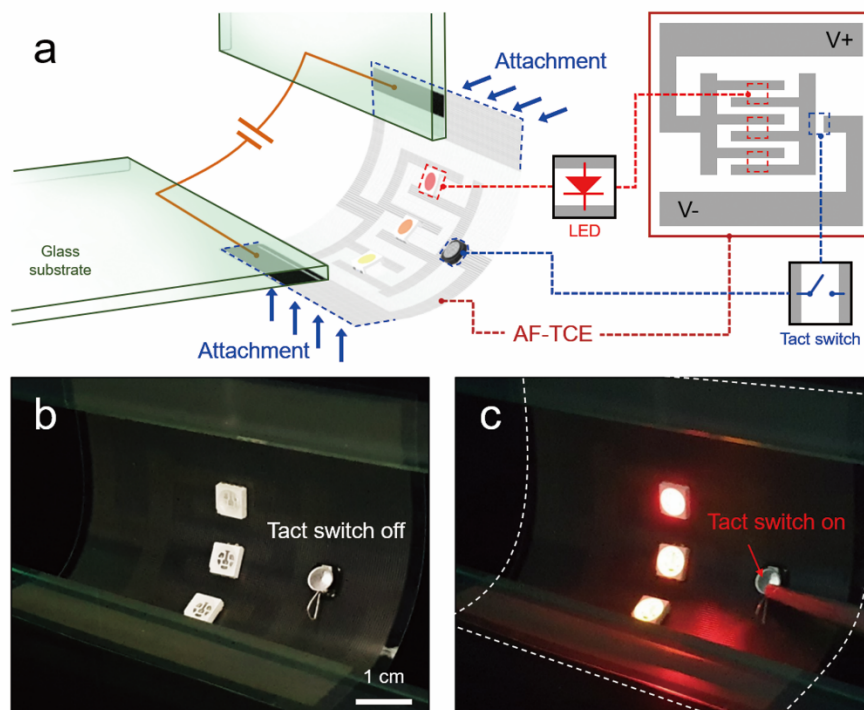
Figure 3.18. AF-TCE smart interconnector with circuit pattern (i) Schematic showing AF-TCE with circuit pattern that is self-attached to vertically- and horizontally-aligned glass substrates. The LEDs and a tact switch can be straightforwardly connected to the circuit with a low preload. (ii, iii) images showing attached LEDs and tact switch in (ii) switch-off and (iii) switch-on states.

3-2-5. Applications of AF-TCE to Transparent Heaters

As a final conceptual demonstration, we utilized the AF-TCE as a flexible transparent attachable resistive heater (**Figure 3.19**). Flexible transparent heaters have attracted substantial attention owing to its high optical transparency and applicability to non-planar surfaces for a wide range of emerging applications including smart windows and personal thermal management.[100,135] This transparent flexible heater also should form conformal mechanical contacts with the target substrates while ensuring stable electrical connections with the metal contact pads used for the application of bias voltage.
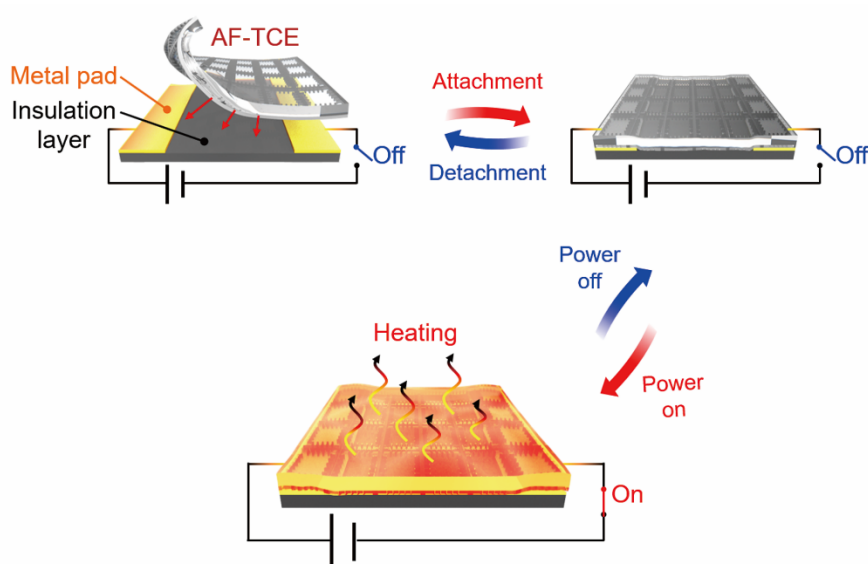
Figure 3.19. Conceptual illustration showing application of AF-TCE as self-attachable flexible heater.

Although previous transparent flexible heaters based on embedded percolating nanowire networks demonstrated superior resistive heating performance even under high mechanical deformation, they did not exhibit self-attachable capability.[100] Accordingly, electrical connections using mechanical clippers (**Figure 3.20a-i**) or Ag paste (**Figure 3.20a-ii**) were typically utilized without effectively considering the interfacing or contact formation technology. We compared the contact formation behavior and Joule-heating performance of the AF-TCE (**Figure 3.20a-iii**) with those of the conventional AgNW-based flexible transparent heaters that were electrically connected using alligator clips and Ag paste (**Figure 3.20a**). The alligator clip-based connection requires substantial space as discussed above. More importantly, the connections were not uniform across the metal pad, and stresses were concentrated at specific points of the pad. Accordingly, non-uniform and localized joule heating was observed across the heater's surface (**Figure 3.20b-i**). In addition, the connection failed at bias voltages above 7 V, revealing the formation of unstable electrical and mechanical contact interfaces. Furthermore, noticeable surface damages of the metal contact pad and substrate were observed after the alligator clips were removed (**Figure 3.20c-i**). When we used the Ag paste, the

heater showed stable Joule-heating performance (**Figure 3.20b-ii**). However, the uncontrollable viscous fluid nature of the Ag paste mostly yielded untidy and thick interfaces with the heater and metal contact pad. Moreover, the Ag paste contact formation is non-reversible, which caused many residues to remain on the contact pads after the removal of the heater from the substrate (**Figure 3.20c-ii**). Furthermore, the whole surface of the nanowire-coated side of the conventional flexible heater could not form close, conformal contacts with the substrates when the alligator clip or Ag paste was utilized.
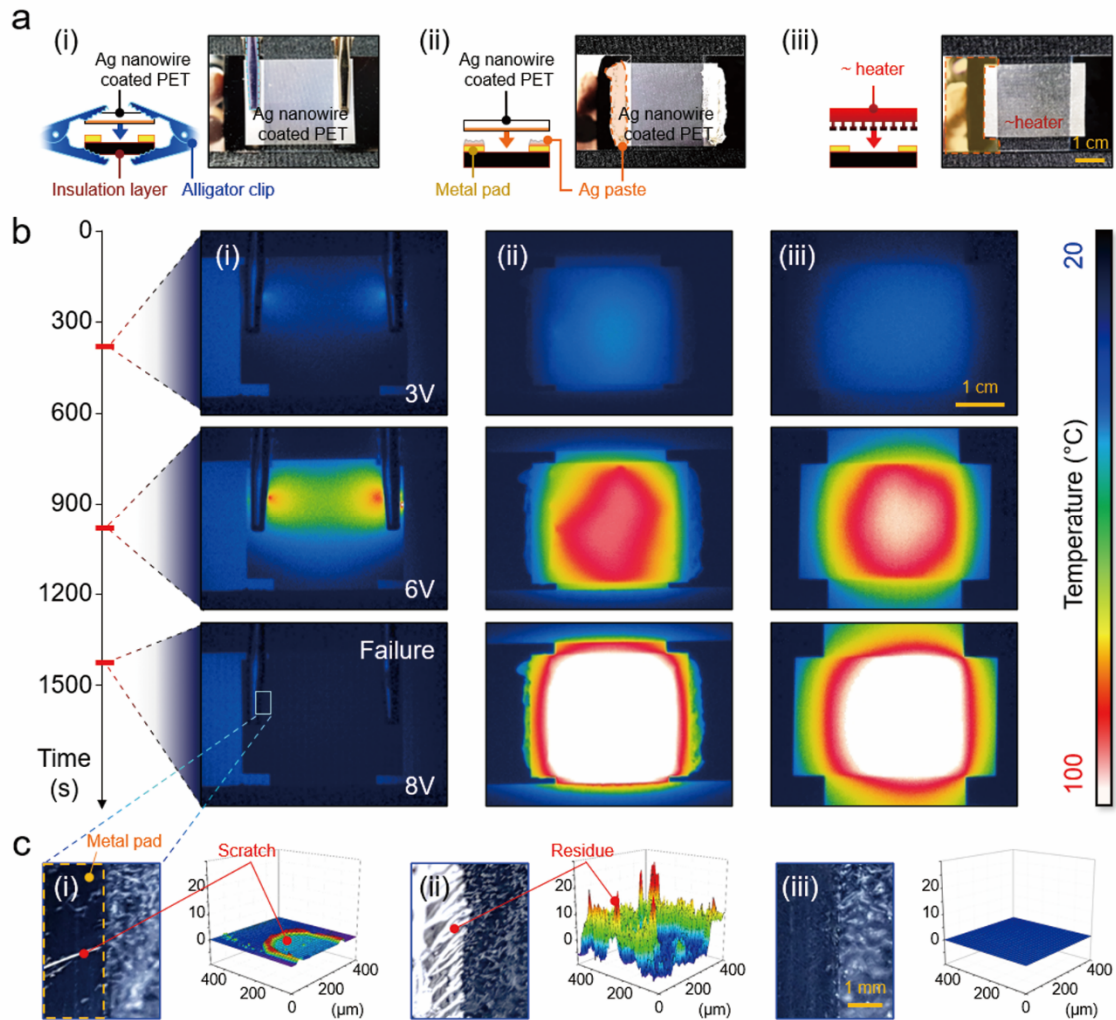
Figure 3.20. Demonstration of AF-TCE-based flexible heater. (a) Electrical connections of conventional flexible heater (AgNW-coated PET film) to metal pads for application of bias voltage using (i) metal clipper and (ii) Ag paste, (iii) electrical connections of AF-TCE to metal pads without using additional devices or materials. (b) IR camera images of conventional heater connected to metal pad formed on a glass substrate using (i) metal clipper, (ii) Ag paste at different bias voltages, (iii) IR camera images of AF-TCE heater attached on a glass substrate with metal pads at different bias voltages. (c) Optical microscopy (left) and 3D profiler (right) images showing the surfaces of metal pads connected with (i) metal clipper, (ii) Ag paste, and (iii) AF-TCE after removal of flexible heaters.

41

In contrast to the conventional flexible heater based on simple AgNW coating, the AF-TCE could form highly uniform and robust electrical and mechanical junctions with the contact pad as well as the whole surface of the substrate (**Figure 3.20a-iii**). Thus, the whole surface of the glass substrate could be uniformly heated with the AF-TCE (**Figure 3.20b-iii**). Moreover, the AF-TCE could form a direct, seamless contact between its nanowire heater and the target substrate. This could provide direct heat-transfer pathways for precise temperature control of the substrate while minimizing energy loss. The nanowires and substrate could be encapsulated by the backing layer of the AF-TCE. This protects them from damage and oxidation and thereby enhances the long-term device stability. Furthermore, the AF-TCE exhibited substantially clean contact interfaces without leaving visible residues on the contact pad and substrate, thereby enabling reversible connections and disconnections (**Figure 3.20c-iii**). **Figure 3.21a** shows the quantitative Joule-heating characteristics of the AF-TCE as a function of the bias voltage. A constant DC bias voltage of 3–7 V was applied between the two metal pads while the active AgNW heater side of the AF-TCE was attached over the substrate. With the voltage application, the average temperature started to increase and attained 32.6 °C, 63.6 °C, and 90.1 °C for applied voltages of 3 V, 5 V, and 7 V, respectively. When the voltage was cut off at 400 s, the temperature decreased rapidly to room temperature (25.0 °C). The AF-TCE showed stable heating performance for stepwise increase in bias voltage from 1 V to 8 V (**Figure 3.21b**). The Joule-heating behavior of the AF-TCE was also stable during the repeated voltage on/off tests at a bias voltage of 5 V (**Figure 3.22**). The heating performance of the AF-TCE heater that was intimately attached to a curved substrate was also demonstrated (**Figure 3.23**).
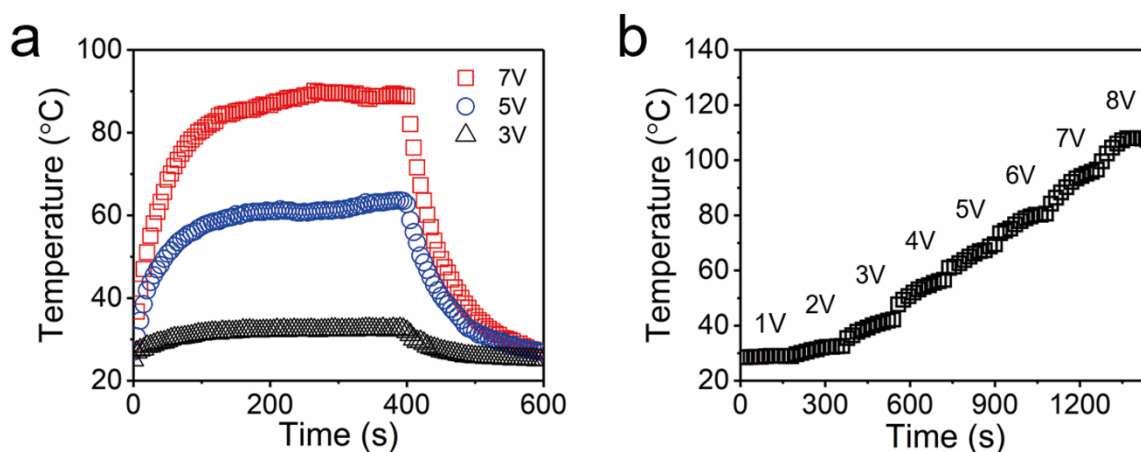
Figure 3.21. Joule-heating characteristics of the AF-TCE (a) Temperature of AF-TCE heater attached on a glass substrate as a function of heating time for different bias voltages. (b) Temperature of AF-TCE attached on a glass substrate as a function of heating time for stepwise increases in bias voltage from 1 V to 8 V.
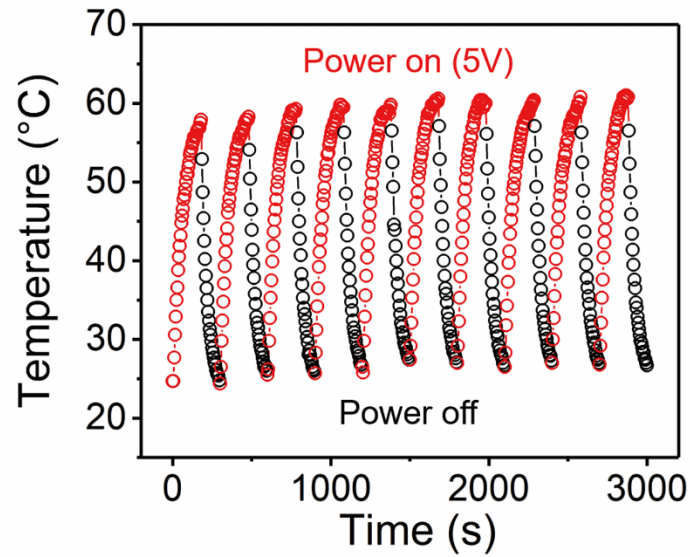
Figure 3.22. Temperature of AF-TCE heater attached on a glass substrate during repeated power-on and -off cycles (bias voltage= 5 V).
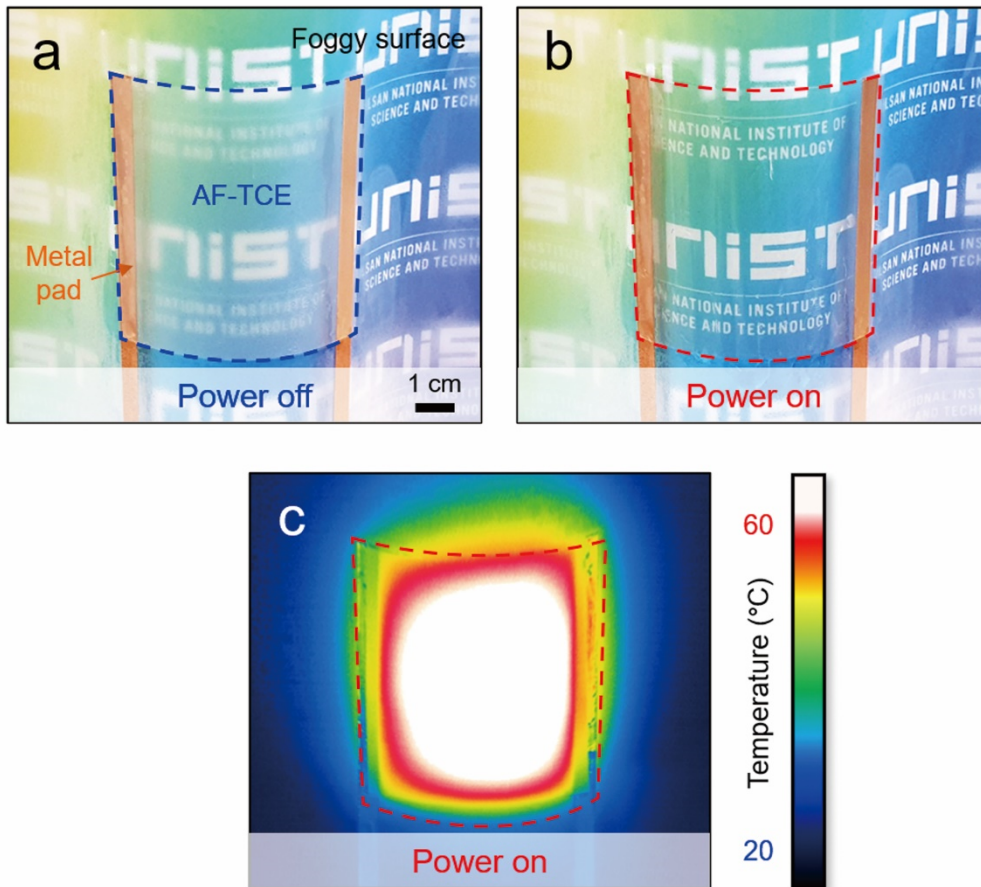
Figure 3.23. Image of the heating performance of the AF-TCE heater. Images showing (a) foggy surface of curved PET film and (b) clear PET film from which steam was removed by AF-TCE heater, (c) IR camera image of AF-TCE conformably attached to curved PET film (applied DC voltage: 5 V).

3-3. Conclusion

In summary, we proposed a flexible transparent conductive electrode that can be strongly attached to planar and non-planar surfaces of flexible devices by integrating bioinspired adhesive architectures and AgNW networks into regular grid patterns. With its high conductivity and strong physical adhesion, the AF-TCE could form stable electrical connections with active components of flexible devices, with highly-controlled, thin, and clean contact interfaces, even under deformation conditions of the AF-TCE. The optical, electrical, and adhesion properties of the AF-TCE could be controlled accurately by modulating the grid pattern, adhesive structures, and deposition dose of AgNWs. Moreover, specific electronic circuits could be generated on the surface of the AF-TCE by selectively depositing AgNWs on its surface. Although we utilized AgNWs, other conducting or semiconducting nanomaterials such as graphene could be utilized for the AF-TCE. Considering that the future development of flexible electronics would require more compact, thinner, damage-free, and highly-controlled contact formation techniques, the AF-TCE is likely to be applied as a smart electrode and interconnect for a wide range of flexible devices including flexible display, flexible transistor, wearable sensors, smart windows, and flexible solar cells.

3-4. Experimental Section

3-4-1. Fabrication of the Self-Attachable, Flexible, Transparent, and Conductive Electrode

The master mold with the negative pattern of the grid with tentacles and tips was prepared on a Si master through photolithography by using a bilayer of photoresist (SU-8 3010, Microchem Corp., USA) and lift-off resist (LOR 10B, Microchem Corp., USA).[69] First, an LOR was spin-coated on a dehydrated Si wafer. This was followed by baking at 200 °C for 10 min. Then, SU-8 photoresist was spin-coated onto the LOR layer and baked at 100 °C for 5 min. The LOR/SU-8-coated wafer was exposed to UV ($\lambda = 365$ nm, dose = 250 mJ cm^{-2}) with a photomask having grid-tentacle patterns. The development of the SU-8 layer using an SU-8 developer (Microchem Corp., USA) for 5 min yielded the negative grid-tentacle patterns. Subsequently, the LOR-layer was selectively removed with an LOR developer (AZ 400K, AZ Electronics Materials Corp., USA) for 40 s to form an undercut of length 3 μm. An AgNW solution (Flexio Corp., Republic of Korea) containing 0.1 wt% AgNWs in DI water with 0.05 wt% hydroxypropyl methylcellulose was then selectively deposited in the trench of the grid pattern. The average diameter and length of the nanowires were 20 nm and 20 μm, respectively. The deposition dose of AgNWs was controlled by modulating the concentration of AgNWs in the solution. The master mold deposited with the AgNW solution was dried at 70 °C for 1 h to remove the remaining solvent. The AgNWs coated over the top surface of the patterned bilayer

(not in the trench) were selectively removed by an adhesive tape. Subsequently, e-PUA solution was prepared by mixing the aliphatic urethane diacrylate oligomer (SC4240, Miwon Specialty Chemical, Republic of Korea) as a prepolymer, to 15 wt% of bisphenol A (ethoxylated) 10 dimetacrylate (BPA(EO)10DMA, M2101, Miwon Specialty Chemical, Republic of Korea) and 6 wt% of tri(propylene glycol) diacrylate (M220, Miwon Specialty Chemical, Republic of Korea).[42] Then, a solution added with 33.3 wt% triton (Triton X-100, Sigma-Aldrich, USA) and 4 wt% of the photoinitiator (Darocur 1173, Ciba Specialty Chemical, Switzerland) was dispensed over the master, and the drop was covered with a PET film. The e-PUA solutions were cured for 30 min by UV irradiation ($\lambda = 365$ nm, dose $= 300$ mJ cm^{-2}). Finally, the cured e-PUA was removed from the master, yielding the AF-TCE. To obtain AF-TCEs with specific circuit patterns for interconnecting LEDs (SMD LED, INC-5450N6PT, Republic of Korea) and a switch (SMD tact switch, TVAF17, China), AgNWs were selectively deposited in the trench of the master mold using a shadow mask with the desired circuit patterns during the fabrication process of the AF-TCE.

3-4-2. Surface and Energy Dispersive Spectroscopy Analyses

SEM and EDS images of the AF-TCE were obtained using an S-4800 microscope (Hitachi, Japan) after coating the AF-TCE with a Pt layer (thickness: 5 nm). AFM images of the AgNWs embedded on the surface of the AF-TCE were obtained with a Multimode V AFM (Veeco, USA) in the tapping mode at a scan rate of 1.0 Hz and a scan resolution of 256×256 pixels. Confocal microscopy images of the AF-TCE samples were obtained using a multi-photon confocal microscope (LSM 780 Configuration 16 NLO, Carl Zeiss, Germany). e-PUA added with rhodamine B (Sigma-Aldrich, USA) was used to fabricate the AF-TCE samples for confocal imaging.

3-4-3. Measurement of Adhesion Strengths of AF-TCE

The adhesion strengths of the AF-TCE were evaluated using custom-built equipment. The equipment has a motorized part movable along the vertical direction. It was connected to a load cell (KTOYO, Republic of Korea). For the adhesion measurement, AF-TCE samples (area: 1×1 cm^2) were mounted on the horizontal surface of the load cell with the samples facing down. The substrates were fixed on a mounting stage of the equipment. The AF-TCEs were then brought in contact with the substrates with a controlled preload. After applying the preloads, an in-plane strain was applied along the vertical direction until the samples were detached from the substrates with a retraction speed of 1 mm s^{-1}. The adhesion measurements were repeated ten times for each sample, and the averaged values are reported.

3-4-4. Measurement of Optical and Electrical Properties of AF-TCE

The optical transmittance of the AF-TCE samples was measured in a wavelength range of 300 to 800 nm using a UV–Vis NIR spectrophotometer (Cary 5000, Agilent, USA). The sheet resistance of the AF-TCEs was measured using a four-point probe surface resistivity meter (CMT-SR1000N, Advanced Instrument Technology, Republic of Korea). The current–voltage characteristics of the AF-TCE in contact with different substrates were measured using a source measure equipment (6430, Keithley, USA). To measure the contact resistances of the AF-TCE, a four-point probe pattern was fabricated by sputtering Au on the glass substrates or PET films connected to the source measure equipment. The contact resistances were measured by attaching AF-TCE on a prepared probe-patterned glass substrate after applying different preloads (0.1–200 kPa). The contact resistance variations of the AF-TCE in contact with the probe-patterned PET film were measured while applying inner or outer bending with different bending curvatures (0–0.67 mm^{-1}). To evaluate the load–current behavior, AF-TCE (area: 1×2 cm^2) was attached on the horizontal flat surface of the load cell with the samples facing down. A glass substrate with two separate pads of sputtered Au (thickness of Au: 100 nm, distance between two pads: 1 cm) was fixed on a mounting stage of the equipment. The adhesive AF-TCE samples were then pressed against the substrate under different applied loads ranging from -100 kPa to 0 kPa. Subsequently, the AF-TCE sample was pulled along the vertical direction until separation occurred with a retraction speed of 0.1 mm s^{-1}. The current across the Au pads was simultaneously measured with the source measure equipment during the loading–unloading cycle. The load–current behavior of the AgNW-coated PET sample ($R_s = 20$ Ω sq^{-1}) was also evaluated as a control for comparison.

3-4-5. Measurement of Joule-Heating Performance of AF-TCE Heater

The AF-TCE heater was attached on a glass substrate with two separated Au electrode pads (thickness of Au: 100 nm, distance between two pads: 1 cm). The temperature variation and IR thermographic data were captured by an infrared (IR) camera (H2640, NEC Avio Infrared Technologies corp., Japan) for different bias voltages (1–8 V). The AgNW-coated planar PET film ($R_s = 20$ Ω sq^{-1})-based heater was used as a control sample for comparison. The AgNW-coated PET film heater was connected to the Au pads using a standard mechanical clipper (i.e., alligator clip) or Ag paste (ELCOAT, CANS, Japan).

3-4-6. Finite Element Analysis (FEA)

FEA analysis was carried out to investigate the adhesive behavior of the AF-TCE with different geometries (G, GT, and GTT) against substrates under mechanical stimuli using general surface-to-

surface contact interaction (COMSOL Multiphysics 5.4, COMSOL Inc., Sweden). We adopted the cohesive zone model (CZM) with the representative volume element (RVE) models and the material properties of the AF-TCE.[136,137] Over 100,000 free tetrahedral elements were employed in the numerical analysis. The loading was simulated by displacement controls of vertical direction to the top surfaces.

Chapter 4. Conclusion and Perspectives

In this dissertation, we proposed novel design strategies for the production of the bioinspired nanocomposite adhesives; 1D nanomaterials are integrated into 3D microarchitectures which allows them to have enhanced thermal or electrical functionality while maintaining superior adhesion performance. This synergetic integration of microstructure and nanomaterials presents a new solution to inherent contact problems of conventional functional adhesives such as surface contamination, damage, and low reusability. The presented production process involving nanomaterial-assisted replica-molding techniques enables the implementation of submicron nanocomposite structures in a precise, simple, and reproducible manner. The superior properties of the produced nanocomposite adhesives have been demonstrated in two potential applications: high-temperature compatible and electrically conductive adhesives, each discussed in the corresponding chapter.

For the high-temperature applications, we proposed thermally stable nanocomposite dry adhesives that are based on the integration of mushroom-like micropillar arrays and MWCNTs. The fabricated nanocomposite dry adhesives made of MWCNT/PDMS mixtures showed notably enhanced thermomechanical stability while maintaining strong adhesion performance even after thermal annealing–cooling cycle at elevated temperatures up to 350 °C. Furthermore, they exhibited superior adhesion performance and heat resistance even under prolonged high-temperature conditions. For the application in advanced electronics, we presented flexible transparent conductive adhesives by integrating tentacle-shaped adhesive architectures with AgNW percolation networks. With their high conductivity and strong physical adhesion, they could form stable electrical connections with active components of flexible devices, with highly controlled, thin, and clean contact interfaces, even under deformation conditions. These properties have been demonstrated in the smart interconnector and self-attachable transparent heater.

In the future, advanced industries will require thinner, more compact, damage-free, and highly controlled contact-formation techniques even in biocompatible and environmentally friendly applications. Considering this, we believe that the proposed nanocomposite adhesive architectures based on maximized van der Waals interactions will become a key component in various next-generation devices. In particular, we expect that the developed strategies for the integration of nanomaterials and microstructures, such as nanomaterial-based molding processes and selective coating, can be extended to various fields since other conducting materials like graphene, metallic nanoparticles, and conductive polymers can be applied to the proposed microstructures. Furthermore, the contamination- or damage-free contact mechanism allows them to become good candidates for skin or tissue adhesives, which will be studied in our future works.

REFERENCES

(1) Zhang, X.; He, J.; Yue, L.; Bai, Y.; Liu, H. Heat Resistance of Acrylic Pressure-Sensitive Adhesives Based on Commercial Curing Agents and UV/Heat Curing Systems. *J. Appl. Polym. Sci.* **2019,** *136*, 47310.

(2) Cui, H.-W.; Kowalczyk, A.; Li, D.-S.; Fan, Q. High Performance Electrically Conductive Adhesives from Functional Epoxy, Micron Silver Flakes, Micron Silver Spheres and Acidified Single Wall Carbon Nanotube for Electronic Package. *Int. J. Adhes. Adhes.* **2013,** *44*, 220–225.

(3) Shuangyan, X.; Dillard, D. A. Determining the Impact Resistance of Electrically Conductive Adhesives using a Falling Wedge Test. *IEEE Trans. Compon. Packaging Technol.* **2003,** *26*, 554–562.

(4) Hsiao, C.-H.; Kung, W.-T.; Song, J.-M.; Chang, J.-Y.; Chang, T.-C. Development of Cu-Ag Pastes for High Temperature Sustainable Bonding. *Mater. Sci. Eng. A-Struct. Mater. Prop. Microstruct. Process.* **2017,** *684*, 500–509.

(5) Yi, H.; Hwang, I.; Sung, M.; Lee, D.; Kim, J.-H.; Kang, S. M.; Bae, W.-G.; Jeong, H. E. Bio-Inspired Adhesive Systems for Next-Generation Green Manufacturing. *Int. J. Precis. Eng. Manuf.-Green Technol.* **2014,** *1*, 347–351.

(6) Marques, E. A. S.; da Silva, L. F. M.; Flaviani, M. Testing and Simulation of Mixed Adhesive Joints for Aerospace Applications. *Compos. Pt. B-Eng.* **2015,** *74*, 123–130.

(7) Wang, Y.; Gozen, A.; Chen, L.; Zhong, W. H. Gum-like Nanocomposites as Conformable, Conductive, and Adhesive Electrode Matrix for Energy Storage Devices. *Adv. Energy Mater.* **2016,** *7*, 1601767.

(8) Laikhtman, A.; Gouzman, I.; Verke, R.; Grossman, E. Contamination Produced by Vacuum Outgassing of Kapton Acrylic Adhesive Tape. *J Spacecraft Rockets* **2009,** *46*, 236-240.

(9) Hassan, J. J.; Mahdi, M. A.; Kasim, S. J.; Ahmed, N. M.; Hassan, H. A.; Hassan, Z. Fast UV Detection and Hydrogen Sensing by ZnO Nanorod Arrays Grown on a Flexible Kapton Tape. *Mater. Sci.* **2013,** *31*, 180–185.

(10) Meschi Amoli, B.; Hu, A.; Zhou, N. Y.; Zhao, B. Recent Progresses on Hybrid Micro–Nano Filler Systems for Electrically Conductive Adhesives (ECAs) Applications. *J. Mater. Sci.-Mater. Electron.* **2015,** *26*, 4730–4745.

(11) Park, Y.-J.; Lim, D.-H.; Kim, H.-J.; Park, D.-S.; Sung, I.-K. UV- and Thermal-Curing Behaviors of Dual-Curable Adhesives Based on Epoxy Acrylate Oligomers. *Int. J. Adhes. Adhes.* **2009,** *29*, 710–717.

(12) Ilyin, S. O.; Brantseva, T. V.; Gorbunova, I. Y.; Antonov, S. V.; Korolev, Y. M.; Kerber, M. L. Epoxy Reinforcement with Silicate Particles: Rheological and Adhesive Properties – Part I: Characterization of Composites with Natural and Organically Modified Montmorillonites. *Int. J. Adhes. Adhes.* **2015,** *61*, 127–136.

(13) Malysheva, G. V.; Bodrykh, N. V. Hot-Melt Adhesives. *Polym. Sci. Ser. D* **2011,** *4*, 301–303.

(14) Sun, S.; Li, M.; Liu, A. A Review on Mechanical Properties of Pressure Sensitive Adhesives. *Int. J. Adhes. Adhes.* **2013,** *41*, 98–106.

(15) Gao, H. J.; Yao, H. M. Shape Insensitive Optimal Adhesion of Nanoscale Fibrillar Structures. *Proc. Natl. Acad. Sci. U. S. A.* **2004,** *101*, 7851–7856.

(16) Baik, S.; Kim, D. W.; Park, Y.; Lee, T. J.; Ho Bhang, S.; Pang, C. A Wet-Tolerant Adhesive Patch Inspired by Protuberances in Suction Cups of Octopi. *Nature* **2017,** *546*, 396–400.

(17) Zhao, Y.; Wu, Y.; Wang, L.; Zhang, M.; Chen, X.; Liu, M.; Fan, J.; Liu, J.; Zhou, F.; Wang, Z. Bio-Inspired Reversible Underwater Adhesive. *Nat. Commun.* **2017,** *8*, 2218.

(18) Eisenhaure, J.; Kim, S. A Review of the State of Dry Adhesives: Biomimetic Structures and the Alternative Designs They Inspire. *Micromachines* **2017,** *8*, 125.

(19) Yu, M. E.; Hwang, J. Y.; Deming, T. J. Role of L-3,4-Dihydroxyphenylalanine in Mussel Adhesive Proteins. *J. Am. Chem. Soc.* **1999,** *121*, 5825–5826.

(20) Tramacere, F.; Kovalev, A.; Kleinteich, T.; Gorb, S. N.; Mazzolai, B. Structure and Mechanical Properties of Octopus Vulgaris Suckers. *J. R. Soc. Interface.* **2014,** *11*, 20130816.

(21) Bae, W. G.; Kim, H. N.; Kim, D.; Park, S. H.; Jeong, H. E.; Suh, K. Y. 25th Anniversary Article: Scalable Multiscale Patterned Structures Inspired by Nature: The Role of Hierarchy. *Adv. Mater.* **2014,** *26*, 675–700.

(22) Autumn, K.; Sitti, M.; Liang, Y. C. A.; Peattie, A. M.; Hansen, W. R.; Sponberg, S.; Kenny, T. W.; Fearing, R.; Israelachvili, J. N.; Full, R. J. Evidence for van der Waals adhesion in gecko setae. *Proc. Natl Acad. Sci. USA* **2002,** *99*, 12252-12256.

(23) Arzt, E.; Gorb, S.; Spolenak, R. From Micro to Nano Contacts in Biological Attachment Devices. *Proc. Natl. Acad. Sci. U. S. A.* **2003,** *100*, 10603–10606.

(24) Autumn, K.; Liang, Y. A.; Hsieh, S. T.; Zesch, W.; Chan, W. P.; Kenny, T. W.; Fearing, R.; Full, R. J. Adhesive Force of a Single Gecko Foot-Hair. *Nature* **2000,** *405*, 681–685.

(25) Carbone, G.; Pierro, E.; Gorb, S. N. Origin of the superior Adhesive Performance of Mushroom-Shaped Microstructured Surfaces. *Soft Matter* **2011,** *7*, 5545–5552.

(26) Jeong, H. E.; Suh, K. Y. Nanohairs and Nanotubes: Efficient Structural Elements for Gecko-Inspired Artificial Dry Adhesives. *Nano Today* **2009,** *4*, 335–346.

(27) Persson, B. N.; Scaraggi, M. Theory of Adhesion: Role of Surface Roughness. *J. Chem. Phys.* **2014,** *141*, 124701.

(28) Northen, M. T.; Greiner, C.; Arzt, E.; Turner, K. L. A Gecko-Inspired Reversible Adhesive. *Adv. Mater.* **2008,** *20*, 3905–3909.

(29) Kim, T.-i.; Jeong, H. E.; Suh, K. Y.; Lee, H. H. Stooped Nanohairs: Geometry-Controllable, Unidirectional, Reversible, and Robust Gecko-like Dry Adhesive. *Adv. Mater.* **2009,** *21*, 2276–2281.

(30) Greiner, C.; Arzt, E.; del Campo, A. Hierarchical Gecko-Like Adhesives. *Adv. Mater.* **2009,** *21*,

479–482.

(31) Jeong, H. E.; Lee, J.-K.; Kim, H. N.; Moon, S. H.; Suh, K. Y. A Nontransferring Dry Adhesive with Hierarchical Polymer Nanohairs. *Proc. Natl. Acad. Sci. U. S. A.* **2009,** *106*, 5639–5644.

(32) Jeong, H. E.; Lee, S. H.; Kim, P.; Suh, K. Y. Stretched Polymer Nanohairs by Nanodrawing. *Nano Lett.* **2006,** *6*, 1508–1513.

(33) del Campo, A.; Greiner, C.; Álvarez, I.; Arzt, E. Patterned Surfaces with Pillars with Controlled 3D Tip Geometry Mimicking Bioattachment Devices. *Adv. Mater.* **2007,** *19*, 1973–1977.

(34) Kwak, M. K.; Jeong, H. E.; Suh, K. Y. Rational Design and Enhanced Biocompatibility of a Dry Adhesive Medical Skin Patch. *Adv. Mater.* **2011,** *23*, 3949–3953.

(35) Boesel, L. F.; Greiner, C.; Arzt, E.; del Campo, A. Gecko-Inspired Surfaces: A Path to Strong and Reversible Dry Adhesives. *Adv. Mater.* **2010,** *22*, 2125–2137.

(36) Kwak, M. K.; Jeong, H. E.; Bae, W. G.; Jung, H. S.; Suh, K. Y. Anisotropic Adhesion Properties of Triangular-Tip-Shaped Micropillars. *Small* **2011,** *7*, 2296–2300.

(37) Jheng, Y.-S.; Lee, Y.-C. Fabrication of Micro/Nano Hierarchical Structures with Analysis on the Surface Mechanics. *Appl. Surf. Sci.* **2016,** *384*, 393–399.

(38) Wang, D.; Zhao, A.; Jiang, R.; Li, D.; Zhang, M.; Gan, Z.; Tao, W.; Guo, H.; Mei, T. Surface Properties of Bionic Micro-Pillar Arrays with Various Shapes of Tips. *Appl. Surf. Sci.* **2012,** *259*, 93–98.

(39) del Campo, A.; Greiner, C.; Arzt, E. Contact Shape Controls Adhesion of Bioinspired Fibrillar Surfaces. *Langmuir* **2007,** *23*, 10235–10243.

(40) Bae, W. G.; Kim, D.; Kwak, M. K.; Ha, L.; Kang, S. M.; Suh, K. Y. Enhanced Skin Adhesive Patch with Modulus-Tunable Composite Micropillars. *Adv. Healthc. Mater.* **2013,** *2*, 109–113.

(41) Zhou, M.; Tian, Y.; Sameoto, D.; Zhang, X.; Meng, Y.; Wen, S. Controllable Interfacial Adhesion Applied to Transfer Light and Fragile Objects by Using Gecko Inspired Mushroom-Shaped Pillar Surface. *ACS Appl. Mater. Interfaces* **2013,** *5*, 10137–10144.

(42) Yi, H.; Hwang, I.; Lee, J. H.; Lee, D.; Lim, H.; Tahk, D.; Sung, M.; Bae, W. G.; Choi, S. J.; Kwak, M. K. *et al.* Continuous and Scalable Fabrication of Bioinspired Dry Adhesives via a Roll-to-Roll Process with Modulated Ultraviolet-Curable Resin. *ACS Appl. Mater. Interfaces* **2014,** *6*, 14590–14599.

(43) Thomas, T. H.; Kendrick, T. C. Thermal Analysis of Polydimethylsiloxanes. I. Thermal Degradation in Controlled Atmospheres. *J. Polym. Sci. Pt. B-Polym. Phys.* **1969,** *7*, 537–549.

(44) Han, D.-H.; Kang, D.-J.; Kang, D.-P.; Min, K.-E. Characteristics of Electrical Insulation in PDMS-ATH Composite for High Voltage Insulators. *Polym. Bull.* **2008,** *61*, 611–617.

(45) Francioso, L.; De Pascali, C.; Bartali, R.; Morganti, E.; Lorenzelli, L.; Siciliano, P.; Laidani, N. PDMS/Kapton Interface Plasma Treatment Effects on the Polymeric Package for a Wearable Thermoelectric Generator. *ACS Appl. Mater. Interfaces* **2013,** *5*, 6586–6590.

(46) Kim, C.-L.; Jung, C.-W.; Oh, Y.-J.; Kim, D.-E. A Highly Flexible Transparent Conductive Electrode Based on Nanomaterials. *NPG Asia Mater.* **2017,** *9*, e438.

(47) Jin, T.; Han, Q.; Wang, Y.; Jiao, L. 1D Nanomaterials: Design, Synthesis, and Applications in Sodium-Ion Batteries. *Small* **2018,** *14*, e1703086.

(48) Garnett, E.; Mai, L.; Yang, P. Introduction: 1D Nanomaterials/Nanowires. *Chem. Rev.* **2019,** *119*, 8955–8957.

(49) Jung, S.-H.; Oh, S.; Kim, S.-W.; Moon, J.-H. Effects of CNT Dosages in Cement Composites on the Mechanical Properties and Hydration Reaction with Low Water-to-Binder Ratio. *Appl. Sci.* **2019,** *9*, 4630.

(50) Li, R. Z.; Hu, A.; Zhang, T.; Oakes, K. D. Direct Writing on Paper of Foldable Capacitive Touch Pads with Silver Nanowire Inks. *ACS Appl. Mater. Interfaces* **2014,** *6*, 21721–21729.

(51) Yu, M. F.; Lourie, O.; Dyer, M. J.; Moloni, K.; Kelly, T. F.; Ruoff, R. S. Strength and Breaking Mechanism of Multiwalled Carbon Nanotubes under Tensile Load. *Science* **2000,** *287*, 637–640.

(52) Kim, Y. A.; Muramatsu, H.; Hayashi, T.; Endo, M.; Terrones, M.; Dresselhaus, M. S. Thermal Stability and Structural Changes of Double-Walled Carbon Nanotubes by Heat Treatment. *Chem. Phys. Lett.* **2004,** *398*, 87–92.

(53) Yun, Y. S.; Kim, D. H.; Kim, B.; Park, H. H.; Jin, H.-J. Transparent Conducting Films Based on Graphene Oxide/Silver Nanowire Hybrids with High Flexibility. *Synth. Met.* **2012,** *162*, 1364–1368.

(54) Zhu, Y.; Qin, Q.; Xu, F.; Fan, F.; Ding, Y.; Zhang, T.; Wiley, B. J.; Wang, Z. L. Size Effects on Elasticity, Yielding, and Fracture of Silver Nanowires: In Situ Experiments. *Phys. Rev. B* **2012,** *85*, 045443.

(55) Liu, C. H.; Yu, X. Silver Nanowire-Based Transparent, Flexible, and Conductive Thin Film. *Nanoscale Res Lett* **2011,** *6*, 1–8.

(56) Xia, H.; Drymiotis, F.; Chen, C.-L.; Wu, A.; Chen, Y.-Y.; Jeffrey Snyder, G. Bonding and High-Temperature Reliability of NiFeMo Alloy/n-Type PbTe Joints for Thermoelectric Module Applications. *J. Mater. Sci.* **2015,** *50*, 2700–2708.

(57) Akram, M.; Jansen, K. M. B.; Ernst, L. J.; Bhowmik, S. Atmospheric Pressure Plasma Surface Modification of Titanium for High Temperature Adhesive Bonding. *Int. J. Adhes. Adhes.* **2011,** *31*, 598–604.

(58) Haddadi, S. A.; Mahdavian-Ahadi, M.; Abbasi, F. Effect of Nanosilica and Boron Carbide on Adhesion Strength of High Temperature Adhesive Based on Phenolic Resin for Graphite Bonding. *Ind. Eng. Chem. Res.* **2014,** *53*, 11747–11754.

(59) Korayem, A. H.; Chen, S. J.; Zhang, Q. H.; Li, C. Y.; Zhao, X. L.; Duan, W. H. Failure of CFRP-to-Steel Double Strap Joint Bonded Using Carbon Nanotubes Modified Epoxy Adhesive at Moderately Elevated Temperatures. *Compos. Pt. B-Eng.* **2016,** *94*, 95–101.

(60) Homma, T.; Yamaguchi, M.; Kutsuzawa, Y.; Otsuka, N. Electrical Stability of Polyimide Siloxane Films for Interlayer Dielectrics in Multilevel Interconnections. *Thin Solid Films* **1999,** *340*, 237–241.

(61) Yu, Y.-Y.; Chien, W.-C.; Tsai, T.-W. High Transparent Soluble Polyimide/Silica Hybrid Optical Thin Films. *Polym. Test.* **2010,** *29*, 33–40.

(62) Ree, M.; Chen, K. J.; Kirby, D. P.; Katzenellbogen, N.; Grischkowsky, D. Anisotropic Properties of High-Temperature Polyimide Thin Films: Dielectric and Thermal-Expansion Behaviors. *J. Appl. Phys.* **1992,** *72*, 2014–2021.

(63) Liao, Y.; Cao, B.; Wang, W.-C.; Zhang, L.; Wu, D.; Jin, R. A Facile Method for Preparing Highly Conductive and Reflective Surface-Silvered Polyimide Films. *Appl. Surf. Sci.* **2009,** *255*, 8207–8212.

(64) Im, H. S.; Kwon, K. Y.; Kim, J. U.; Kim, K. S.; Yi, H.; Yoo, P. J.; Pang, C.; Jeong, H. E.; Kim, T. I. Highly Durable and Unidirectionally Stooped Polymeric Nanohairs for Gecko-Like Dry Adhesive. *Nanotechnology* **2015,** *26*, 415301.

(65) Zhang, Y.; Lo, C. W.; Taylor, J. A.; Yang, S. Replica molding of high-aspect-ratio polymeric nanopillar arrays with high fidelity. *Langmuir* **2006,** *22*, 8595-8601.

(66) Jin, K.; Tian, Y.; Erickson, J. S.; Puthoff, J.; Autumn, K.; Pesika, N. S. Design and Fabrication of Gecko-Inspired Adhesives. *Langmuir* **2012,** *28*, 5737–5742.

(67) Ye, Z.; Lum, G. Z.; Song, S.; Rich, S.; Sitti, M. Phase Change of Gallium Enables Highly Reversible and Switchable Adhesion. *Adv. Mater.* **2016,** *28*, 5088–5092.

(68) Ho, A. Y. Y.; Yeo, L. P.; Lam, Y. C.; Rodriguez, I. Fabrication and Analysis of Gecko-Inspired Hierarchical Polymer Nanosetae. *ACS Nano* **2011,** *5*, 1897-1906.

(69) Yi, H.; Kang, M.; Kwak, M. K.; Jeong, H. E. Simple and Reliable Fabrication of Bioinspired Mushroom-Shaped Micropillars with Precisely Controlled Tip Geometries. *ACS Appl. Mater. Interfaces* **2016,** *8*, 22671–22678.

(70) Murphy, M. P.; Kim, S.; Sitti, M. Enhanced Adhesion by Gecko-Inspired Hierarchical Fibrillar Adhesives. *ACS Appl. Mater. Interfaces* **2009,** *1*, 849–855.

(71) Huber, G.; Mantz, H.; Spolenak, R.; Mecke, K.; Jacobs, K.; Gorb, S. N.; Arzt, E. Evidence for capillarity contributions to gecko adhesion from single spatula nanomechanical measurements. *Proc. Natl Acad. Sci. USA* **2005,** *102*, 16293-16296.

(72) Lee, E.; Yang, S. Bio-Inspired Responsive Polymer Pillar Arrays. *MRS Commun.* **2015,** *5*, 97–114.

(73) Li, M.; Zhao, A.; Jiang, R.; Wang, D.; Li, D.; Guo, H.; Tao, W.; Gan, Z.; Zhang, M. Regulation of the Elastic Modulus of Polyurethane Microarrays and Its Influence On Gecko-Inspired Dry Adhesion. *Appl. Surf. Sci.* **2011,** *257*, 3336–3340.

(74) Qu, L.; Dai, L. Gecko-Foot-Mimetic Aligned Single-Walled Carbon Nanotube Dry Adhesives

with Unique Electrical and Thermal Properties. *Adv. Mater.* **2007,** *19*, 3844–3849.

(75) Norkhairunnisa, M.; Azizan, A.; Mariatti, M.; Ismail, H.; Sim, L. C. Thermal Stability and Electrical Behavior of Polydimethylsiloxane Nanocomposites with Carbon Nanotubes and Carbon Black Fillers. *J. Compos. Mater.* **2011,** *46*, 903–910.

(76) Dumas, L.; Bonnaud, L.; Olivier, M.; Poorteman, M.; Dubois, P. Multiscale Benzoxazine Composites: The Role of Pristine CNTs as Efficient Reinforcing Agents for High-Performance Applications. *Compos. Pt. B-Eng.* **2017,** *112*, 57–65.

(77) Camino, G.; Lomakin, S. M.; Lazzari, M. Polydimethylsiloxane Thermal Degradation - Part 1. Kinetic Aspects. *Polymer* **2001,** *42*, 2395–2402.

(78) Zhao, Y.-H.; Zhang, Y.-F.; Bai, S.-L.; Yuan, X.-W. Carbon Fibre/Graphene Foam/Polymer Composites with Enhanced Mechanical and Thermal Properties. *Compos. Pt. B-Eng.* **2016,** *94*, 102–108.

(79) Pan, Y.-T.; Wang, X.; Li, Z.; Wang, D.-Y. A Facile Approach towards Large-Scale Synthesis of Hierarchically Nanoporous SnO2@Fe2O3 0D/1D Hybrid and Its Effect on Flammability, Thermal Stability and Mechanical Property of Flexible Poly(vinyl chloride). *Compos. Pt. B-Eng.* **2017,** *110*, 46–55.

(80) Camino, G.; Lomakin, S. M.; Lageard, M. Thermal polydimethylsiloxane degradation. Part 2. The degradation mechanisms. *Polymer* **2002,** *43*, 2011-2015.

(81) Silva, V. P.; Gonçalves, M. C.; Yoshida, I. V. P. Biogenic Silica Short Fibers as Alternative Reinforcing Fillers of Silicone Rubbers. *J. Appl. Polym. Sci.* **2006,** *101*, 290–299.

(82) Chin, P.; McCullough, R. L.; Wu, W.-L. An Improved Procedure for Determining the Work of Adhesion for Polymer-Solid Contact. *J. Adhes.* **1997,** *64*, 145–160.

(83) Gorb, S.; Varenberg, M.; Peressadko, A.; Tuma, J. Biomimetic Mushroom-Shaped Fibrillar Adhesive Microstructure. *J. R. Soc. Interface.* **2007,** *4*, 271–275.

(84) Johnston, I. D.; McCluskey, D. K.; Tan, C. K. L.; Tracey, M. C. Mechanical Characterization of Bulk Sylgard 184 for Microfluidics and Microengineering. *J. Micromech. Microeng.* **2014,** *24*, 035017.

(85) Xue, C.; Du, G. Q.; Chen, L. J.; Ren, J. G.; Sun, J. X.; Bai, F. W.; Yang, S. T. A Carbon Nanotube Filled Polydimethylsiloxane Hybrid Membrane for Enhanced Butanol Recovery. *Sci. Rep.* **2014,** *4*, 5925.

(86) Meng, H.; Sui, G. X.; Xie, G. Y.; Yang, R. Friction and Wear Behavior of Carbon Nanotubes Reinforced Polyamide 6 Composites under Dry Sliding and Water Lubricated Condition. *Compos. Sci. Technol.* **2009,** *69*, 606–611.

(87) Xiong, W.; Liu, H.; Chen, Y.; Zheng, M.; Zhao, Y.; Kong, X.; Wang, Y.; Zhang, X.; Kong, X.; Wang, P. *et al.* Highly Conductive, Air-Stable Silver Nanowire@Iongel Composite Films toward Flexible Transparent Electrodes. *Adv. Mater.* **2016,** *28*, 7167–7172.

54

(88) Liu, N.; Chortos, A.; Lei, T.; Jin, L. H.; Kim, T. R.; Bae, W. G.; Zhu, C. X.; Wang, S. H.; Pfattner, R.; Chen, X. Y. *et al.* Ultratransparent and Stretchable Graphene Electrodes. *Sci. Adv.* **2017,** *3*, e1700159.

(89) Kim, K. K.; Ha, I.; Won, P.; Seo, D. G.; Cho, K. J.; Ko, S. H. Transparent Wearable Three-Dimensional Touch by Self-Generated Multiscale Structure. *Nat. Commun.* **2019,** *10*, 2582.

(90) Jeon, I.; Yoon, J.; Kim, U.; Lee, C.; Xiang, R.; Shawky, A.; Xi, J.; Byeon, J.; Lee, H. M.; Choi, M. *et al.* High-Performance Solution-Processed Double-Walled Carbon Nanotube Transparent Electrode for Perovskite Solar Cells. *Adv. Energy Mater.* **2019,** *9*, 1901204.

(91) Song, W. G.; Kwon, H.-J.; Park, J.; Yeo, J.; Kim, M.; Park, S.; Yun, S.; Kyung, K.-U.; Grigoropoulos, C. P.; Kim, S. *et al.* High-Performance Flexible Multilayer MoS2 Transistors on Solution-Based Polyimide Substrates. *Adv. Funct. Mater.* **2016,** *26*, 2426–2434.

(92) Niu, Z.; Cui, F.; Kuttner, E.; Xie, C.; Chen, H.; Sun, Y.; Dehestani, A.; Schierle-Arndt, K.; Yang, P. Synthesis of Silver Nanowires with Reduced Diameters Using Benzoin-Derived Radicals to Make Transparent Conductors with High Transparency and Low Haze. *Nano Lett.* **2018,** *18*, 5329–5334.

(93) Mardiansyah, D.; Badloe, T.; Triyana, K.; Mehmood, M. Q.; Raeis-Hosseini, N.; Lee, Y.; Sabarman, H.; Kim, K.; Rho, J. Effect of Temperature on the Oxidation of Cu Nanowires and Development of an Easy to Produce, Oxidation-Resistant Transparent Conducting Electrode Using a PEDOT:PSS Coating. *Sci. Rep.* **2018,** *8*, 10639.

(94) Kang, S.; Cho, S.; Shanker, R.; Lee, H.; Park, J.; Um, D. S.; Lee, Y.; Ko, H. Transparent and Conductive Nanomembranes with Orthogonal Silver Nanowire Arrays for Skin-Attachable Loudspeakers and Microphones. *Sci. Adv.* **2018,** *4*, eaas8772.

(95) An, B. W.; Heo, S.; Ji, S.; Bien, F.; Park, J.-U. Transparent and Flexible Fingerprint Sensor Array with Multiplexed Detection of Tactile Pressure and Skin Temperature. *Nat. Commun.* **2018,** *9*, 2458.

(96) Yokota, T.; Zalar, P.; Kaltenbrunner, M.; Jinno, H.; Matsuhisa, N.; Kitanosako, H.; Tachibana, Y.; Yukita, W.; Koizumi, M.; Someya, T. Ultraflexible Organic Photonic Skin. *Sci. Adv.* **2016,** *2*, e1501856.

(97) Xiong, J.; Li, S.; Ye, Y.; Wang, J.; Qian, K.; Cui, P.; Gao, D.; Lin, M. F.; Chen, T.; Lee, P. S. A Deformable and Highly Robust Ethyl Cellulose Transparent Conductor with a Scalable Silver Nanowires Bundle Micromesh. *Adv. Mater.* **2018,** *30*, e1802803.

(98) Cho, S.; Kang, S.; Pandya, A.; Shanker, R.; Khan, Z.; Lee, Y.; Park, J.; Craig, S. L.; Ko, H. Large-Area Cross-Aligned Silver Nanowire Electrodes for Flexible, Transparent, and Force-Sensitive Mechanochromic Touch Screens. *ACS Nano* **2017,** *11*, 4346–4357.

(99) Jang, J.; Hyun, B. G.; Ji, S.; Cho, E.; An, B. W.; Cheong, W. H.; Park, J.-U. Rapid Production of Large-Area, Transparent and Stretchable Electrodes Using Metal Nanofibers as Wirelessly

Operated Wearable Heaters. *NPG Asia Mater.* **2017,** *9*, e432.

(100) Hong, S.; Lee, H.; Lee, J.; Kwon, J.; Han, S.; Suh, Y. D.; Cho, H.; Shin, J.; Yeo, J.; Ko, S. H. Highly Stretchable and Transparent Metal Nanowire Heater for Wearable Electronics Applications. *Adv. Mater.* **2015,** *27*, 4744–4751.

(101) Zhao, D.; Zhang, C.; Kim, H.; Guo, L. J. High-Performance Ta2O5/Al-Doped Ag Electrode for Resonant Light Harvesting in Efficient Organic Solar Cells. *Adv. Energy Mater.* **2015,** *5*, 1500768.

(102) Lee, S.; Lee, J. S.; Jang, J.; Hong, K.-H.; Lee, D.-K.; Song, S.; Kim, K.; Eo, Y.-J.; Yun, J. H.; Gwak, J. *et al.* Robust Nanoscale Contact of Silver Nanowire Electrodes to Semiconductors to Achieve High Performance Chalcogenide Thin Film Solar Cells. *Nano Energy* **2018,** *53*, 675–682.

(103) Lee, E.; Ahn, J.; Kwon, H.-C.; Ma, S.; Kim, K.; Yun, S.; Moon, J. All-Solution-Processed Silver Nanowire Window Electrode-Based Flexible Perovskite Solar Cells Enabled with Amorphous Metal Oxide Protection. *Adv. Energy Mater.* **2018,** *8*, 1702182.

(104) Tian, L.; Zimmerman, B.; Akhtar, A.; Yu, K. J.; Moore, M.; Wu, J.; Larsen, R. J.; Lee, J. W.; Li, J.; Liu, Y. *et al.* Large-Area MRI-Compatible Epidermal Electronic Interfaces for Prosthetic Control and Cognitive Monitoring. *Nat. Biomed. Eng.* **2019,** *3*, 194–205.

(105) Kim, M. K.; Parasuraman, R. N.; Wang, L.; Park, Y.; Kim, B.; Lee, S. J.; Lu, N.; Min, B.-C.; Lee, C. H. Soft-Packaged Sensory Glove System for Human-like Natural Interaction and Control of Prosthetic Hands. *NPG Asia Mater.* **2019,** *11*, 43.

(106) Cao, Y.; Tan, Y. J.; Li, S.; Lee, W. W.; Guo, H.; Cai, Y.; Wang, C.; Tee, B. C. K. Self-Healing Electronic Skins for Aquatic Environments. *Nat. Electron.* **2019,** *2*, 75–82.

(107) Li, H.; McRae, L.; Firby, C. J.; Al-Hussein, M.; Elezzabi, A. Y. Nanohybridization of Molybdenum Oxide with Tungsten Molybdenum Oxide Nanowires for Solution-Processed Fully Reversible Switching of Energy Storing Smart Windows. *Nano Energy* **2018,** *47*, 130–139.

(108) Wang, Y.; Kim, J. C.; Wu, R. J.; Martinez, J.; Song, X.; Yang, J.; Zhao, F.; Mkhoyan, A.; Jeong, H. Y.; Chhowalla, M. Van der Waals Contacts between Three-Dimensional Metals and Two-Dimensional Semiconductors. *Nature* **2019,** *568*, 70–74.

(109) Wang, Q.; Xu, K.; Wang, Z.; Wang, F.; Huang, Y.; Safdar, M.; Zhan, X.; Wang, F.; Cheng, Z.; He, J. Van der Waals Epitaxial Ultrathin Two-Dimensional Nonlayered Semiconductor for Highly Efficient Flexible Optoelectronic Devices. *Nano Lett.* **2015,** *15*, 1183–1189.

(110) Andrews, J. B.; Mondal, K.; Neumann, T. V.; Cardenas, J. A.; Wang, J.; Parekh, D. P.; Lin, Y.; Ballentine, P.; Dickey, M. D.; Franklin, A. D. Patterned Liquid Metal Contacts for Printed Carbon Nanotube Transistors. *ACS Nano* **2018,** *12*, 5482–5488.

(111) Ko, D.; Gu, B.; Kang, S. J.; Jo, S.; Hyun, D. C.; Kim, C. S.; Kim, J. Critical Work of Adhesion for Economical Patterning of Silver Nanowire-Based Transparent Electrodes. *J. Mater. Chem. A* **2019,** *7*, 14536–14544.

(112) Brand, M. J.; Kolp, E. I.; Berg, P.; Bach, T.; Schmidt, P.; Jossen, A. Electrical Resistances of

Soldered Battery Cell Connections. *J. Energy Storage* **2017,** *12*, 45–54.

(113) Sung, I. H.; Kim, J. W.; Noh, H. J.; Jang, H. Effect of Displacement and Humidity on Contact Resistance of Copper Electrical Contacts. *Tribol. Int.* **2016,** *95*, 256–261.

(114) Yun, J. Ultrathin Metal Films for Transparent Electrodes of Flexible Optoelectronic Devices. *Adv. Funct. Mater.* **2017,** *27*, 1606641.

(115) Spyropoulos, G. D.; Ramirez Quiroz, C. O.; Salvador, M.; Hou, Y.; Gasparini, N.; Schweizer, P.; Adams, J.; Kubis, P.; Li, N.; Spiecker, E. *et al.* Organic and Perovskite Solar Modules Innovated by Adhesive Top Electrode and Depth-Resolved Laser Patterning. *Energy Environ. Sci.* **2016,** *9*, 2302–2313.

(116) Poppinga, S.; Hartmeyer, S. R.; Seidel, R.; Masselter, T.; Hartmeyer, I.; Speck, T. Catapulting Tentacles in a Sticky Carnivorous Plant. *PLoS One* **2012,** *7*, e45735.

(117) Krausko, M.; Perutka, Z.; Sebela, M.; Samajova, O.; Samaj, J.; Novak, O.; Pavlovic, A. The Role of Electrical and Jasmonate Signalling in the Recognition of Captured Prey in the Carnivorous Sundew Plant Drosera Capensis. *New Phytol.* **2017,** *213*, 1818–1835.

(118) Sitti, M.; Fearing, R. S. Synthetic Gecko Foot-Hair Micro/Nano-Structures as Dry Adhesives. *J. Adhes. Sci. Technol.* **2003,** *17*, 1055–1073.

(119) Zhou, Y.; Layani, M.; Wang, S.; Hu, P.; Ke, Y.; Magdassi, S.; Long, Y. Fully Printed Flexible Smart Hybrid Hydrogels. *Adv. Funct. Mater.* **2018,** *28*, 1705365.

(120) Seong, M.; Lee, J.; Hwang, I.; Jeong, H. E. Significant Adhesion Enhancement of Bioinspired Dry Adhesives by Simple Thermal Treatment. *Int. J. Precis. Eng. Manuf.-Green Technol.* **2019,** *6*, 587–599.

(121) Jang, K. I.; Li, K.; Chung, H. U.; Xu, S.; Jung, H. N.; Yang, Y.; Kwak, J. W.; Jung, H. H.; Song, J.; Yang, C. *et al.* Self-Assembled Three Dimensional Network Designs for Soft Electronics. *Nat. Commun.* **2017,** *8*, 15894.

(122) Ha, M.; Lim, S.; Cho, S.; Lee, Y.; Na, S.; Baig, C.; Ko, H. Skin-Inspired Hierarchical Polymer Architectures with Gradient Stiffness for Spacer-Free, Ultrathin, and Highly Sensitive Triboelectric Sensors. *ACS Nano* **2018,** *12*, 3964–3974.

(123) Sun, K.; Ko, H.; Park, H.-H.; Seong, M.; Lee, S. H.; Yi, H.; Park, H. W.; Kim, T. I.; Pang, C.; Jeong, H. E. Hybrid Architectures of Heterogeneous Carbon Nanotube Composite Microstructures Enable Multiaxial Strain Perception with High Sensitivity and Ultrabroad Sensing Range. *Small* **2018,** *14*, e1803411.

(124) Li, X.; Lee, H. K.; Phang, I. Y.; Lee, C. K.; Ling, X. Y. Superhydrophobic-Oleophobic Ag Nanowire Platform: An Analyte-Concentrating and Quantitative Aqueous and Organic Toxin Surface-Enhanced Raman Scattering Sensor. *Anal. Chem.* **2014,** *86*, 10437–10444.

(125) Wang, G.; Bi, L.; Wei, W.; Zhang, X.; Gu, Y.; Huang, L.; Yin, H.; Li, Y.; Chen, G.; Wu, Z. *et al.* Strongly Adhesive Silver Nanowire Ink Makes Delamination-Free Transparent Conductive Films

Possible. *ACS Appl. Nano Mater.* **2019,** *2*, 6707–6714.

(126) Park, J.; Lee, K.; Um, H.-D.; Kim, K.-H.; Seo, K. Direct Fabrication of Flexible Ni Microgrid Transparent Conducting Electrodes via Electroplated Metal Transfer. *Adv. Mater. Technol.* **2018,** *3*, 1700213.

(127) De, S.; Coleman, J. N. Are There Fundamental Limitations on the Sheet Resistance and Transmittance of Thin Graphene Films? *ACS Nano* **2010,** *4*, 2713–2720.

(128) De, S.; King, P. J.; Lyons, P. E.; Khan, U.; Coleman, J. N. Size Effects and the Problem with Percolation in Nanostructured Transparent Conductors. *ACS Nano* **2010,** *4*, 7064–7072.

(129) Ellmer, K. Past Achievements and Future Challenges in the Development of Optically Transparent Electrodes. *Nat. Photon.* **2012,** *6*, 809–817.

(130) Xie, S.; Li, T.; Xu, Z.; Wang, Y.; Liu, X.; Guo, W. A High-Response Transparent Heater Based on a CuS Nanosheet Film with Superior Mechanical Flexibility and Chemical Stability. *Nanoscale* **2018,** *10*, 6531–6538.

(131) Yi, H.; Lee, S. H.; Ko, H.; Lee, D.; Bae, W. G.; Kim, T. i.; Hwang, D. S.; Jeong, H. E. Ultra-Adaptable and Wearable Photonic Skin Based on a Shape-Memory, Responsive Cellulose Derivative. *Adv. Funct. Mater.* **2019,** *29*, 1902720.

(132) Hu, H.; Tian, H.; Shao, J.; Li, X.; Wang, Y.; Wang, Y.; Tian, Y.; Lu, B. Discretely Dupported Dry Adhesive Film Inspired by Biological Bending Behavior for Enhanced Performance on a Rough Surface. *ACS Appl. Mater. Interfaces* **2017,** *9*, 7752–7760.

(133) Nam, S.; Song, M.; Kim, D. H.; Cho, B.; Lee, H. M.; Kwon, J. D.; Park, S. G.; Nam, K. S.; Jeong, Y.; Kwon, S. H. *et al.* Ultrasmooth, Extremely Deformable and Shape Recoverable Ag Nanowire Embedded Transparent Electrode. *Sci. Rep.* **2014,** *4*, 4788.

(134) Guimaraes, M. H.; Gao, H.; Han, Y.; Kang, K.; Xie, S.; Kim, C. J.; Muller, D. A.; Ralph, D. C.; Park, J. Atomically Thin Ohmic Edge Contacts between Two-Dimensional Materials. *ACS Nano* **2016,** *10*, 6392–6399.

(135) Hazarika, A.; Deka, B. K.; Kim, D.; Jeong, H. E.; Park, Y. B.; Park, H. W. Woven Kevlar Fiber/Polydimethylsiloxane/Reduced Graphene Oxide Composite-Based Personal Thermal Management with Freestanding Cu-Ni Core-Shell Nanowires. *Nano Lett.* **2018,** *18*, 6731–6739.

(136) Wang, D.; Ba, D.; Hao, M.; Duan, Q.; Liu, K.; Mei, Q. A Numerical Insight into Elastomer Normally Closed Micro Valve Actuation with Cohesive Interfacial Cracking Modelling. *Appl. Surf. Sci.* **2018,** *440*, 84–90.

(137) Li, Q.; Peer, A.; Cho, I. H.; Biswas, R.; Kim, J. Replica Molding-Based Nanopatterning of Tribocharge on Elastomer with Application to Electrohydrodynamic Nanolithography. *Nat. Commun.* **2018,** *9*, 974.

Acknowledgments

There was a lot of support for my achievements in graduate studies. Thus, I would like to express my deep gratitude to everyone who helped me with my doctoral research.

First, I would like to express my greatest appreciation to my advisor, Prof. Hoon Eui Jeong, for giving me valuable motivation and support. Even before I became a graduate student, he allowed me to experience various fields of research beyond mechanical engineering and guided me to develop a variety of skills and the mindset of a researcher. In particular, he taught me how to approach the research and describe the results effectively, which will be a great support in my life. Once again, I would like to show my sincerest gratitude to my advisor for providing me with such valuable opportunities and experiences.

I would also like to express my gratitude to the rest of the committee members: Prof. Taesung Kim, Prof. Hyung Wook Park, Prof. Heungjoo Shin, and Prof. Moon Kyu Kwak. Their valuable and constructive comments enriched my research and allowed me to look at my research objectively and critically. I appreciate their sincere advice and encouragement.

I would like to express my gratitude to the MBM laboratory members who, as graduate students, spent the most time together. Hoon Yi, Hyun-Ha Park, and Han-Gil Ko, as good seniors, have helped me to learn new things on countless occasions. They taught me the basic skills through their research and were willing to share many concerns and difficulties. The precious and pleasant research experiences with these three people with different thoughts and personalities have helped me mature mentally. Insol Hwang supported me as a thoughtful and kind colleague who shared most of my research. We dealt with many research projects together, which greatly extended my knowledge. I appreciate all the experiences and achievements that we had together. Kahyun Sun, Sang-Hyeon Lee, and Minsu Kang gave me dedicated support based on their knowledge of other research fields. We shared constructive opinions in various discussions through which I extended my research background as well as found beneficial solutions to the problems I faced. I would also like to sincerely thank Hyun-Wook Ko, Joosung Lee, Jaeil Kim, Geonjun Choi, Hyejin Jang, and Seongjin Park. Even though we spent a short time together, their great and dedicated support has been of great help to me. Moreover, their valuable perspectives and new ideas were very stimulating and inspirational for me. I sincerely cheer and support all the members who have already graduated and those who will lead the laboratory in the future.

I would like to thank all my friends, seniors, and juniors for being a strong support in my graduate life. In addition, I appreciate other laboratory members in UNIST for their generous and valuable help with my research.

Last but not least, I sincerely thank my parents, Wookhwan Seong and Kyungja Park, and my brother Hyojung Seong for their continuous trust, devoted support, and infinite love.